People's Democratic Republic of Algeria
Ministry of Higher Education and Scientific Research

University M'Hamed BOUGARA – Boumerdes

Institute of Electrical and Electronic Engineering

Department of Electronics

Final Year Project Report Presented in Partial Fulfilment of the Requirements for the Degree of

MASTER

In **Electronics**

Option: **Computer Engineering**

Title:

Implementation of deterministic and probabilistic fiber tracking algorithms for abnormal brain tissues analysis using dMRI

Presented by:

- **MOUSSAOUI Imane**

Supervisor:

Dr. CHERIFI Dalila

Registration Number:...../2019

List of Figures

List of Tables

Contents

Acknowlegement

This humble work would not have been possible without the help and support of many people. First and foremost, I would like to thank my supervisor, Dr CHERIFI Dalila . Not only she gave me the opportunity to dive in a field, the least to say about, is intersting but also she was my second mom in the institute. Without her support I would not have been able to complete this work in time. Words cannot express my gratitude to her.
I would also like to thank my family for their love and support. My achievements are, no small part, due to their encouragement. In particular, I would like to thank my parents Mohamed and Yakout, for their love, inspiration and unfaltering guidance, which encouraged me to through my years of study and my brothers Aymen and Anas and my sister Ihcen for staying by my side in my difficult moments.
I like to thank Dr. Terchi for his help in writing the report.
A special thanks goes to BENOUADEH Sara alumnus at INELEC for her help , support, time and patience.
Additional debts are owed to Dr. DERICHE Rachid, research director at INRIA in the Sophia Antipolis-Méditérannée Research Center for importing the diffusion MRI technique to algeria with the same quality of what is done abroad, and GERARD Gabriel, researcher at Sherbrooke Connectivity Imaging Lab (SCIL), University of Sherbrooke-Canada, for his priceless suggestions and remarks on our work.
I am grateful to Dr. Debiane for his contribution and Dr Kechih for examining our results and providing us with medical explanations would thank them for their time and patience.
I thank Professor ELETHERIOS Garyfallidis the founder of Dipy for his answers and his modesty and patience with me as a new member in the field.
I would like to thank my friends at the Institute and outside for their help, support and for believing in me. Every small word has its effect on this work.

Finally I would like to thank Mr A. ALILECHE for his help in so many ways and for his time and patience.

Abstract

Diffusion magnetic resonance imaging (DMRI) is a technique that allows to probe the microstructure of materials. In our case we use it for the White Matter (WM) while tractography is a computational reconstruction method based on diffusion-weighted magnetic resonance imaging (DWI)that attempts to reveal the trajectories of white matter pathways in vivo and to infer the underlying structural connectome of the human brain. The aim of our study is to reach the best reconstruction of the WM in the presence of abnormal tissues such as Astrocytoma type II and III, Glioblastoma Multiform, Meningioma and Oligodendrocytoma type II. For that purpose, nine data about the mentioned diseases aquired from the the UK data archive are utilised, the procedure is to apply both deterministic and probabilistic methods with two stopping criteria for each to the dataset. The analysis of the four outputs is conducted for each patient to assess the results in the region of interest (ROI).

Besides the comparison between the tracts generated with the probabilistic and the deterministic algorithms, another comparison is performed for FA=0.2 and FA=0.4 as stopping criteria and their effect on the generated fibers.

The main contribution of this work is the implementation of the probabilistic tracking algorithm. While searching for information concerning tractography .It is found that deterministic tractography is widely used because of its ease and simplicity. In this repport advantages of using the probabilistic method for better results demonstrated therefore both methods were applied on the same dataset in addition to analising the effect of stopping criterion on the results in the ROI and the whole brain.

List of abbreviations

ADC	: Apparent Diffusion Component
CC	: Corpus Callosum
CSD	: Constrained Spherical Deconvolution
CT	: Computer Tomograpgy
CSF	: Cerebrospinal Fluid
DIPY	: Diffusion Imaging in Python
dMRI	: Diffusion Magnetic Resonance Imaging
dODF	: Diffusion Orientation Distribution Function
DSI	: Diffusion Spectrum Imaging
DTI	: Diffusion Tensor Imaging
DWI	: Diffusion weighted Imaging
FA	: Fractional Anisotropy
FACT	: Fiber Assignment by Continuous Tracking
FOD	: Fiber Orientation Density
fODF	: fiber Orientation Density Function
FRT	: Funk-Radon transform
GM	: Grey Matter
HARDI	: High Angular Resolution Diffusion Imaging
MD	: Mean Diffusivity
MI-Brain	: Medical Imaging Brain
MRI	: Magnetic Resonance Imaging
NMR	: Nuclear Magnetic Resonance
PDF	: Probability Density Function
QBI	: Q-ball Imaging
RK4	: Runge-Kutta 4
ROI	: Region Of Interest
SD	: Spherical Deconvolution

SD : Standard Deviation

SH : Spherical Harmonics

TEND : Tensor Deflection

WM : White Matter

UODF : Uncertainty Orientation Distribution Function

General Introduction

Imaging of the brain has been a challenge for all imaging modalities from the beginning of radiology. Its bony box makes it completely unapproachable to physical exam. Currently the most utilized modalities in neuroimaging are computer tomograpgy (CT), MRI and angiography .

Traditional MRI images present white matter as a homogeneous structure. In reality, fiber tracts originate from various sources, radiate in different orientations, and travel to distinct regions of the brain. Diffusion MRI provides investigators with the opportunity to visualize these different white matter pathways and study the complexities of axonal architecture in *vivo* and a *non-invasive* way.

Diffusion magnetic resonance imaging (MRI) records the motion of water molecules in the brain and based on this information, the microstructure of the brain tissue through which the water is moving is inferred.

The main clinical application of the diffusion MRI is the study of the neurogical disorders, especially for the management of patients with acute stroke, because it can reveal abnormalities in white matter fiber structure and provide models of brain connectivity.

The remainder of the present is organised along the lines of the following structure.

The first chapter is about diffusion MRI's general aspects; concepts and mechanism. the second chapter demonstrates the available reconstruction techniques thier mathematical representations and limitations. The third chapter is about deterministic and probabilistic tractography. the rest is the experimental part the results and conclusions.

Chapter 1

Diffusion MRI

1.1 Introduction

Neuroimaging, also known as brain imaging, is the use of various techniques to directly or indirectly image the structure, function or pharmacology of the nervous system. It is a relatively new discipline within medicine, neuroscience, and psychology.
Diffusion MRI is a magnetic resonance imaging method which came into existence in the mid-1980s , it allows the mapping of the diffusion process of molecules, mainly water, in biological tissue, in *vivo* and non-invasively. Molecular diffusion in tissue is not free, but reflects interactions with many obstacles , such as macromolecules, fibers, mambrance. Water molecules diffusion patterns can therefore reveal microscopic details about the tissue architecture.

1.2 Brain anatomy

The microscopic level of the brain at consists of three types of tissues grey matter, white matter and verticle shown in figure 1.1:

- **Grey matter**: Grey matter has a pinkish-greyish coulor in the living brain, contains the cell bodies, the dendrites and the neuron axon terminals of neurons as shown in figure 1.2.
- **White matter**: is made of axons connecting different parts of grey matter to each other.
- **Ventricle**: is a communicating network of cavities filled with cerebrospinal fluid (CSF) and located within the brain parenchyma.

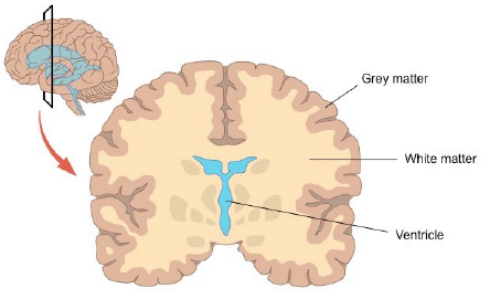

Figure 1.1: Coronal section of the brain

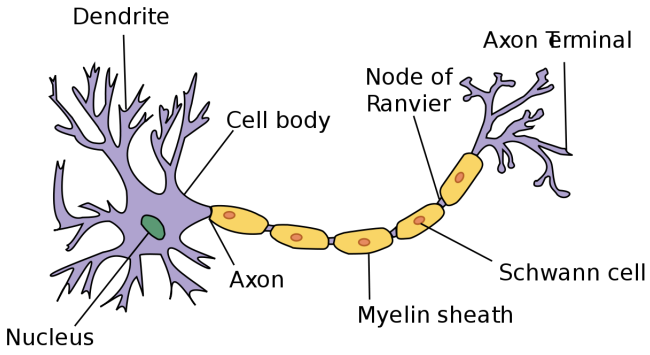

Figure 1.2: Structure of a neuron

1.3 MRI mechanism

The magnetic resonance (MR) process can simply be regarded to be to be a simple reemission phenomenon. Energy is applied to a patient to be reemitted, detected, and processed.

The MR process is based on the interaction between a strong, external magnetic field (B_0) and the magnetic spin of nuclei of the tissue of interest inside the gantry. The tissue nuclei themselves act as tiny magnets. When the tissue of interest is placed in the strong external magnetic field, the nuclei of the tissue are aligned along this very powerful magnetic field, producing an equilibrium magnetization of the tissue. Such tissue magnetization is then disrupted by properly tuned radio frequency (RF) pulses. When the RF pulse is turned off, the nuclei recover ("relax") to equilibrium in the main magnetic field, producing in the process RF signals.

The RF signals produced by tissue relaxation are proportional to the magnitude of the initial alignment, to the tissue proton density , and to the different rates at which nuclei of a distinct chemistry and chemical surrounding relax. The differences in the RF signals measured can be used to calculate a grey scale for image presentation ("tissue contrast"). In order to obtain a significant difference in tissue contrast, the signals are measured, or read out, after a user-defined time has elapsed from the initial RF excitation. This time span is called the relaxation time (TR) and is - like all time measurements in MRI sequences - measured in milliseconds. The image is mathematically constructed from the signal using Fourier transformation.

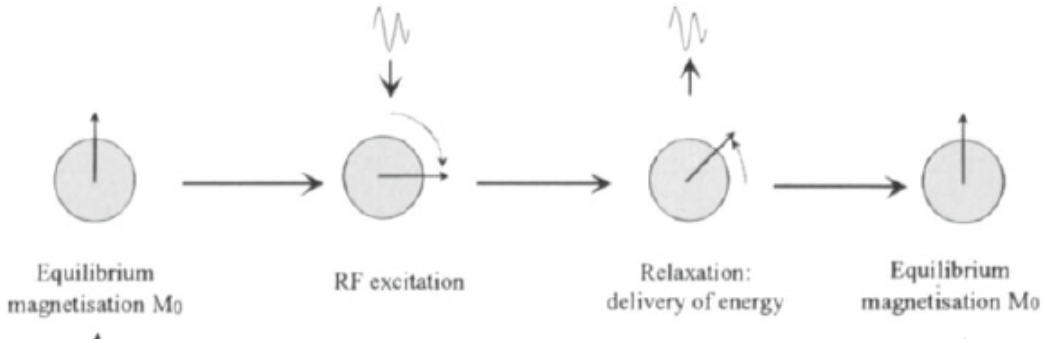

Figure 1.3: Magnetic resonance cycle

1.4 Diffusion

Diffusion refers to the random, microscopic movement of water and other small molecules due to thermal collisions. Diffusion, also known as Brownian motion, is named in honor of the scottish botanist Robert Brown who first observed spontaneous vibration of pollen particles under the microscope in 1827 [2]. Diffusion was described later by the Fick's first law [11].

$$J = -D\nabla C \tag{1.1}$$

Where:
J is the net particle flux (unit:mol/m^2s), C is the particle concentration (unit:mol/m^3), and D is the diffusion coefficent (unit:m^2/s).

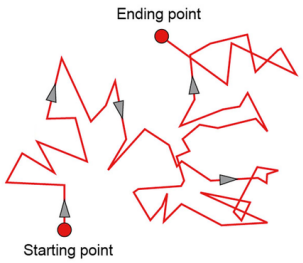

Figure 1.4: Simulation of Brownian motion of a particle at starting point t_0 and ending point t_1 .

The concentration changes as a function of time as shown in figure 1.5.

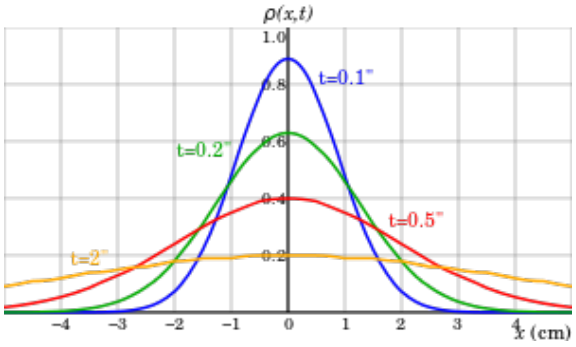

Figure 1.5: Characteristic bell-shaped curves of the diffusion of Brownian particles

The problem with Fick's first law (1.1) is that when the concentration gradient vanishes, no flux should result. This leads one to conclude that the diffusion stopped. However the thermal collisions and diffusion still continue, simply they cancelling each other. Einstein combined his theory of "random walk" with principle of fluidic friction developed in the 19th century by George Stokes resulting in Stokes-Einstein equation.

$$D = \frac{KT}{6\pi r\eta} \tag{1.2}$$

where:

D is the diffusion coefficient (unit:m^2/s), T is the absolute temperature (unit:k), KBoltzmann's constant (unit:J/k), r is the radius of the particle, η is the dynamic viscosity.

In 1905 Albert Einstein incorporated Fick's first law and developed a comprehensive equation in answer to the question "how far a Brownian particle moves in a given period of time ?" He introduced the equation for the diffusion probability density function which is able to predict the displacement given a period of time [5].

$$p(r,t) = \frac{1}{\sqrt{4\pi tD}^3} e^{-\frac{\|r^2\|}{4tD}} \tag{1.3}$$

where:

D is the diffusion coefficient (unit:m^2/s), r is the displacement vector (unit:m), t is the time (unit:s).

From equation (1.3), Einstein's equation can derive the relation between the mean root square and the diffusion coefficient.

$$\|r^2\| = 6Dt \tag{1.4}$$

Diffusion is called isotropic when particals are free to move in all directions and this motion can be characterized by a single diffusion coefficient(D), and it is called anisotropic when the diffusion varies with the direction this motion can be characterized by a 3×3 matrix.

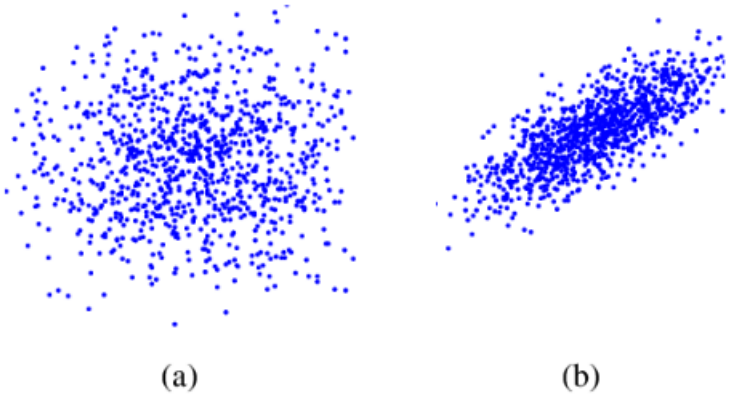

Figure 1.6: Diffusion;(a) isotropic diffusion and (b) anisotropic diffusion.

1.5 Diffusion Weighted Imaging

Diffusion Weighted Imaging (DWI) is a crutial part of modern MRI imaging and is really an integral part of imaging almost all the brain pathologies. It seeks to measure the ease with which water molecules are able to diffuse in any particular voxel therefore, it provides us an insight into, essentially, the histology of that tissue, how cellular it is, what the extracellular space is, what the intercellular space is. This can be very usuful in distinguishing, for example, various entities as well as tumour grading.
The most commonly used terminology is whether or not a brain mass or a region demonstrates restricted diffusion, which indicates the location of abnormally decreased diffusivity compared to what that tissue should exhibit .

1.5.1 Pulse Gradient Spin Echo

In an environment where diffusion of water molecules is hindered by the biological structure of the tissue, we can only infer the mean displacement. Therefore, we measure the Apparent Diffusion Coefficient (ADC) which determines the percentage of isotropy from which conclusions about the micro-architecture can be made.

To calculate the ADC parameter, it is required to sensitize water molecules in the brain. From the direction of the applied gradients, we can then detect different values along different directions [20].

The excitation pulse used in DWI is based on measurements which are influenced by spin motion. We apply an initial gradient of determined intensity (G) and duration (δ) that offsets the phase of all the spins in a voxel; time TE/2 corresponds to the application of a 180° RF pulse that inverts the phase of the population of spins. After a certain time lapse (Δ) from the first gradient, another one, of inverse polarity, is applied causing the spins to rephase. However, spins move from original position retaining a residual phase offset that allows diffusion quantification [23].

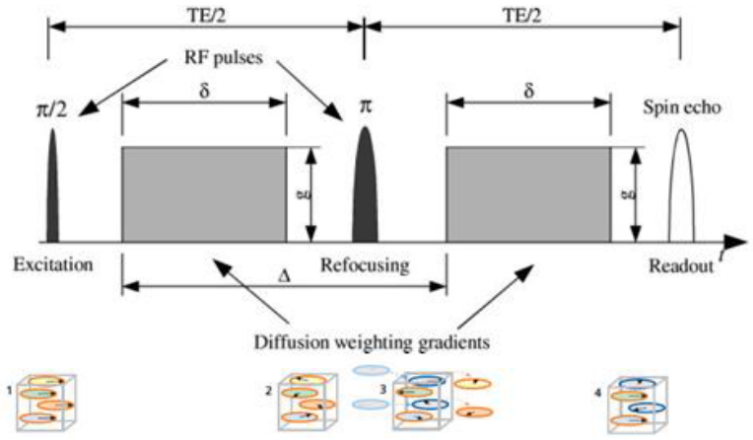

Figure 1.7: Pulse Gradient Spin Echo

1.5.2 Diffusion weighted imaging and b-values relationship

The b-value is a factor that reflects the strength and timing of the gradients used to generate diffusion-weighted iamges [17]. The higher the b-value the stronger the diffusion effects.

The term "b-value" is derived from Stejskal and Tanner 1965 landmark paper in which they discribed their pulsed gradient diffusion method .

This technique still forms the basis for most modern DWI pulse sequences and consists

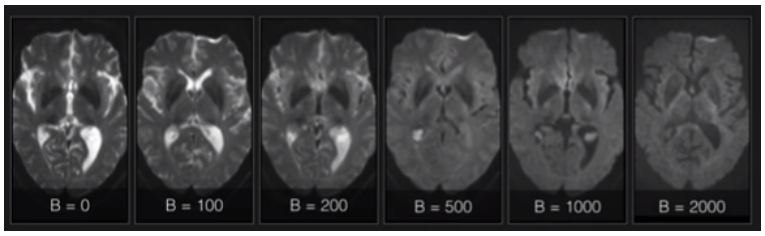

Figure 1.8: Brain DWI with different b-values (0,100,200,500,1000 and 2000 s/mm^2)

of two gradient pulses of magnitude (G) and duration (δ) separated by time interval (Δ).

$$b = \gamma^2 G^2 \delta^2 (\Delta - \frac{\delta}{3}) \tag{1.5}$$

Where:

γ is the proton gyromagnetic ratio .

The question of what b-value is optimal is still unresolved, the problem is that this value depends on many factors such as the target of reconstruction .

It has shown that a value satisfying $(b \times ADC) \approx 1$ is generally close to optimal for the tensor-based measures such as anisotropy and mean diffusivity. However in crossing fibre context, higher b-values in range of $2500 - 3000 s/mm^2$have been shown to provide better angular resolution, Those b-values are acheivable on modern clinical systems, their use reduces the overall signal to noise ratio(SNR) of the images compared to lower b-values, this reduction is partly a consequence of the longer echo time required to accommodate inevitably longer DW gradients leading to signal loss through T_2 decay [7].

Specifically, if s_0 is the MR signal at baseline and D is the diffusion coefficient, the signal s after the diffusion gradients have been applied is given by :

$$s = s_0 e^{-bD} \tag{1.6}$$

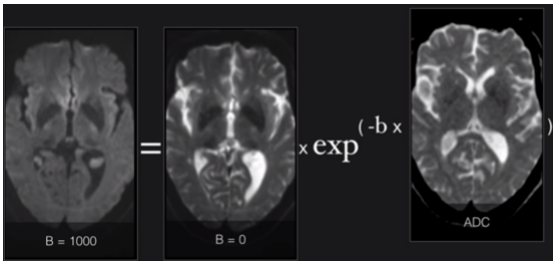

Figure 1.9: The relation of the weighted image with the b-value

1.6 Summary

In this chapter we introduced a brief history of neuroimaging from the ordinary MRI. Then we presented the diffusion MRI technique; its mechanism and the idea of following the water molecules to probe the brain tissue and some physics of pulse gragient spin echo and we defined also some related scalars input such as b-value and output such as fractional anisotropy and what they reffer to.

Chapter 2

Reconstruction Methods

2.1 Introduction

The data extracted from the diffusion MRI provides essential information like the fractional anisotropy and the main diffusion direction, such information enables the estimation of the fiber orientation of the the WM. However those data can't be directly used by clinicians, therefore, they should be preceded by some reconstruction techniques represent these data in the image space.

In this chapter, we will introduce Diffusion tensor imaging (DTI) and High angular resolution imaging (HARDI) techniques and discuss their respective advantages and limitations.

2.2 Diffusion Tensor Imaging and tensor model

"Diffusion Tensor Imaging is a cutting edge imaging technique that provides quantitive information with which we visualize and study connectivity and continuity of neural pathways in the central and peripheral nervous system in *vivo* [1].

For routine DWI, the complexity of diffusion in biological tissues is often reduced to a single average value. A superior method to model diffusion is to use the diffusion tensor, a $[3 \times 3]$ reflecting diffusion in different directions [19].

$$D = \begin{pmatrix} D_{xx} & D_{xy} & D_{xz} \\ D_{yx} & D_{yy} & D_{yz} \\ D_{zx} & D_{zy} & D_{zz} \end{pmatrix} \tag{2.1}$$

The three elements on the diagonal (D_{xx}, D_{yy}, D_{zz}) represent diffusion measured along each of the principal axes (x, y, z) .

The six remaining elements are symmetric and reflect the correlation of the random motion between each pair of principal directions .

For perfect isotropic diffusion

$$D_{isotropic} = \begin{pmatrix} D_{xx} & 0 & 0 \\ 0 & D_{yy} & 0 \\ 0 & 0 & D_{zz} \end{pmatrix} \tag{2.2}$$

Where $D_{xx} = D_{yy} = D_{zz}$. For anisotropic diffusion, diagoanl elements are unequal and the off-diagonal elements have non-vanishing values.

Fortunately, there exists optimal cordinate system based on the diffusion ellipsoid, whose main axis is parallel to the principal diffusion direction within a voxel with axes parallel and tangent to the principal directions of diffusion.

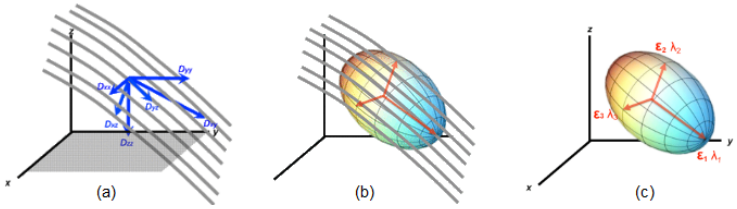

Figure 2.1: Ellipsoid model using eigenvalues $(\lambda_1, \lambda_2, \lambda_3)$ and eigenvectors $(\varepsilon_1, \varepsilon_2, \varepsilon_3)$

The eigenvectors ε give the directions in which the ellipsoid has major axes, and the corresponding eigenvalues λ give the magnitude of the peak in that direction .

2.2.1 Tensor estimation

DTI technique relies on the mathematics and physical representations of geometric quantities known as tensors which can be calculated from DWI data collected with diffusion sensitizing gradients in at least six different directions. though in practical cases more directions are needed to improve accuracy.

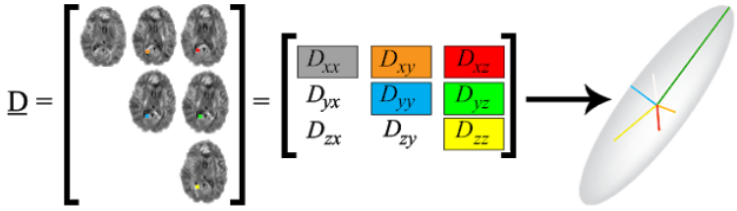

Figure 2.2: From diffusion image to tensor

The diffusion tensor is represented in 3×3 symmetric matrix as shown in fig 2.3, where $D_{XY} = D_{YX}$,$D_{XZ} = D_{ZX}$ and $D_{YZ} = D_{ZY}$. This means that the diffusion tensor matrix is symmetric with only 6 unique elements. To estimate all of them, a minimum of 7 measurements are needed: one baseline (b_0) and 6 source data sets.
The diffusion tensor is usually calculated from diffusion weighted images (DWI) by solving

the Stejskal-Tanner equation

$$S_k = S_0 e^{-bg_k^T D g_k} \tag{2.3}$$

where g is the gradient direction is written as :

$$g = \begin{pmatrix} g_x \\ g_y \\ g_z \end{pmatrix} \tag{2.4}$$

g^T is the transpose of g and D is the diffusion tensor.
The solution for the estimated tensor is shown in appendix A.

2.3 Diffusion Tensor Imaging measurements

After the estimation of the diffusion tensor useful quantities can be extracted from the eigenvalues and the eigenvectors such as the apparent diffusion coefficient (ADC) and the fractional anisotropy (FA) these are used to create images reflecting the various diffusion properties of a tissue.
For a more insighted understanding of the relation of the eigenvalues and the eigenvectors with the diffusion tensor, the diffusion matrix is decomposed as shown in equation 2.5.

$$D = V\Lambda V^T = \begin{pmatrix} e_1 & e_2 & e_3 \end{pmatrix} \begin{pmatrix} \lambda_1 & 0 & 0 \\ 0 & \lambda_2 & 0 \\ 0 & 0 & \lambda_3 \end{pmatrix} \begin{pmatrix} e_1 \\ e_2 \\ e_3 \end{pmatrix} \tag{2.5}$$

where:

$$V = \begin{pmatrix} e_1 & e_2 & e_3 \end{pmatrix}$$

$$\Lambda = \begin{pmatrix} \lambda_1 & 0 & 0 \\ 0 & \lambda_2 & 0 \\ 0 & 0 & \lambda_3 \end{pmatrix}$$

2.3.1 Fractional anisotropy

There is no one-to-one relationship between a given anatomical feature and a particular MR measure. However, fractional anisotropy (FA) is usually sensitive to several tissue characteristics, like myelination, axon diameter, fiber density and fiber organization, which have to be interpreted carefully.

FA is calculated from the eigenvalues $(\lambda_1, \lambda_2, \lambda_3)$ of the diffusion tensor using the following equation:

$$FA = \sqrt{\frac{3}{2}} \sqrt{\frac{(\lambda_1 - MD)^2 + (\lambda_2 - MD)^2 + (\lambda_3 - MD)^2}{\lambda_1^2 + \lambda_2^2 + \lambda_3^2}} \tag{2.6}$$

where MD is the mean diffusivity and calculated as follow:

$$MD = \frac{\lambda_1 + \lambda_2 + \lambda_3}{3} \tag{2.7}$$

The value of FA lies between zero and one, a value of zero means that the diffusion is isotropic $(\lambda_1 = \lambda_2 = \lambda_3)$, while a value of one means that the diffusion occurs along one axis and is totally rectricted in other directions.

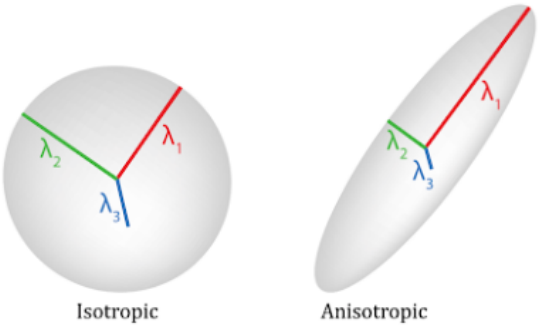

Figure 2.3: Eigenvalues in isotropic and anisotropic diffusion

2.4 Diffusion Tensor scalars and brain structure

It is important, while working with DTI, to understand what is being measured and how it is related to the biological microstructure of the brain.

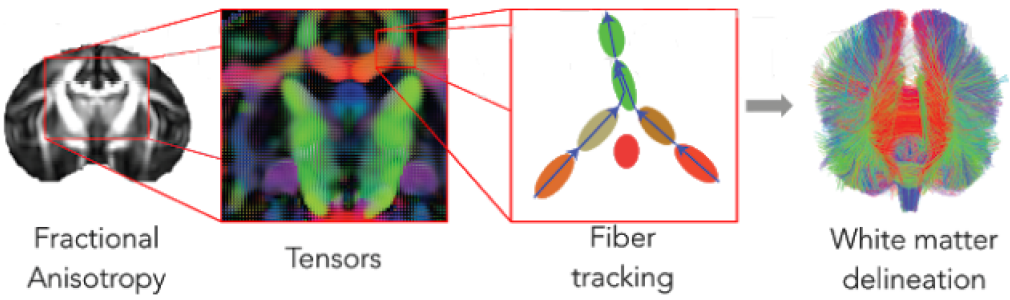

Figure 2.4: Utilization of Fractional Anisotropy technique in determining pathologies

Some DTI scalars are listedtogether with the information they provide:

- Fractional Anisotropy (FA) is a summary measure of microstructural integrity. While FA is highly sensitive to microstructural changes, it is less depending on the type of change.
- Mean Diffusivity (MA) is an inverse measure of the membrane density. It is very similar for both GM and WM and higher for CSF. MD is sensitive to cellularity, edema, and necrosis.
- Axial Diffusivity (AD) tends to be variable in WM changes and pathology. AD decreases in axonal injury. The ADs of WM tracts have been reported to increase with brain maturation.
- Radial Diffusivity (RD) increases in WM with de- or dys-myelination. RD may also be influencedby changes in the axonal diameters in the axonal diameters or density may also influence RD. The relation between DTI scalars and neural microstructure is summarized in (table 2.1).

Table 2.1: relaion between DTI scalars and neural microstructure.

	FA	MD	AD	RD
Gray Matter	↓	-	↓	↑
White Matter	↑	-	↑	↓
CSF	↓	↑	↑	↑
High Myelination	↑	↓	-	↓
Dense axonal packing	↑	↓	-	↓
WM Maturation	↑	↓	↑	↓
Axonal degeneration	↓	↑	↓	↑
Demyelination	↓	↑	-	↑

2.5 Diffusion Tensor Imaging limitations

DTI technique, proposed in 1992 and 1993 andnbased on the fundamental discovery of Douek et al, Basser et al is widely used to reconstruct the micro-architecture of brain tissue because it requires a short aquisition time (approximately 5 min) and it is available on most clinical systems. Yet, it suffers serious limitations in regions of crossing fibers (fig 2.5); it cannot represent multiple, independent intra-voxel orientations. Therefore estimated directions may be ambiguous and misleading in voxels with complex fiber structure especially that the crossing fibers affects as much as 90% of all voxels in the brain [14].

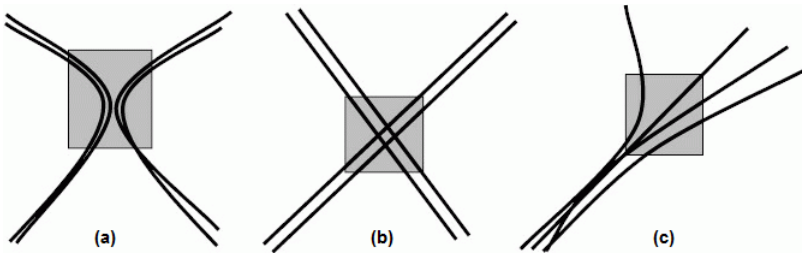

Figure 2.5: Limitations of DTI a) kissing fibers, b) crossing fibers, c)branching fibers.

2.6 High Angular Resolution Diffusion Techniques

HARDI technique was originally developed to overcome the DTI limitation and make the tractography more robust thanks to its capability of resolving crossing, kissing and branching fibers as shown in (fig 2.6). This feature is crucial for studies of brain connectivity[22]. It requires the aquisition of over 50 gradients and high b-value while DTI only requires 6 gradients and thus a minimum of six diffusion-weighted images is required in addition to a baseline S_0 image using low b-values. Since more measurements are required, a better reconstruction would result. This is achieved at the price of more time being required for the measurement acquisition.

Figure 2.6: Difference between the a) DTI and b) HARDI.

HARDI methods fall into two broad approaches

- Model-free approaches relie on extracting orientation density function directly from the collected data
- Model-based approaches consist of applying a model to the data before extracting the fiber orientation distribution

2.6.1 Q-space

For all the model-based approaches, the number of diffusion measurements needed equals, in theory, the number of parameters for the model. For example three tensors (three ellipsoids) require 18 independent measurement (six to each tensor) but when no model is used, the estimation of fibers orientation requires the characterization of a 3D measure-

ment of the diffusion process. For that 3D measurements for water molecules displacement are needed in each voxel, as shown in (fig 15). The signal generated from the latter measurements is called the q-space signal(Callaghan 1991) [8] .

2.6.2 Acquisition strategies

The acquisition strategy for HARDI is typicaly asociated with spherical sampling schemes, though there exist other sampling schemes like Cartesian, radial, and other sampling schemes in general 3D diffusion imaging shown in figure 16.

The two major sampling strategies shown in 17 are:

- Sampling the q-space on a dense 3D cartesian grid. This technique is generally associated with Diffusion Spectrum Imaging (DSI) .
- Single shell spherical sampling for a single b-value in q-space. If multiple b-values are used, it is called multishell HARDI, and it is used specially for Q-ball imaging technique.

The first technique is based on estimating the PDF after sampling a large number of q-space points then taking the inverse of Fourier transform. This method requires the use of very high magnetic gradients and is mainly used in Diffusion Spectrum Imaging (DSI). The second technique consists of estimating the Orientation Distribution Function (ODF) by sampling on a spherical shell of radius determined by the used b-value and is the core of q-ball imaging.

2.6.3 Diffusion Signal and Diffusion Propagation

It was shown that the relation 2.8 is true only if the diffusion gradient is infinitely small, or is called the narrow pulse approximation.

$$E(q,t) = \int_{R^3} p(r,t) e^{-2\pi i q^T r} dr \tag{2.8}$$

Theoritically, the relation 2.8 is Fourier Transform and it imposes to sample the full q-space which is not possible practically. In our context and for the purpose of diffusion imaging and HARDI, the most important thing to know is that there is a Fourier transform relationship between the q-space and the diffusion signal that we measure. The real space probability distribution function that describes the diffusion process of water molecules, also called the diffusion propagator.

2.6.4 Diffusion Spectrum Imaging (DSI)

Diffusion spectrum imaging (DSI) is a technique that is capable of mapping fibre architectures by imaging the 3D spectra of water molecules' displacement. First, it is known that the signal obtained for each voxel is proportional to the average displacement of spins. By assuming that the duration of the gradient is negligible compared to the mixing time (time between the 2 gradient), then the relation 2.8 is true; which leads to:

$$p(r,t) = F^{-1}(E(q,t)) \tag{2.9}$$

$$\psi(\theta,\phi) = \int_0^\infty p(r,\theta,\phi)r^2 dr \quad ST : \theta \in [0,\pi], \phi \in [0,2\pi] \tag{2.10}$$

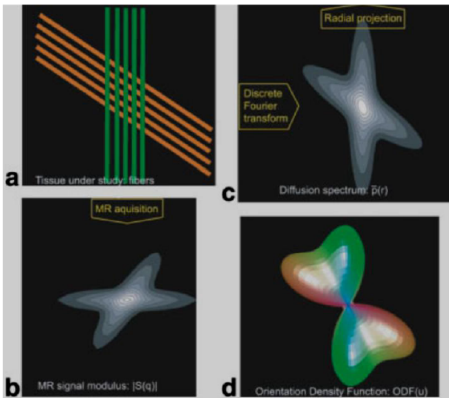

Figure 2.7: Reconstruction of the diffusion ODF from DSI A) Tissue under study – crossing fibres. B) Voxel expectation of the signal – diffusion spectrum. C) Fourier Transform application to diffusion spectrum– diffusion spectra. D) Angular structure of diffusion.

This method requires fairly a strong imaging gradients ($500 \leq b \leq 20{,}000$ s/mm2) in addition to a long acquisition time to measure hundreds of diffusion directions and "b-values" (in the range of 150–515 measurements) that cover the 3D Cartesian grid which make it clinically infeasible. But there are active developments of new pulse sequences and new undersampling schemes to make DSI possible in less than 20 min.

2.6.4.1 Orientation Diffusion Function (ODF)

The diffusion orientation distribution function is the most famous feature of the diffusion propagator, ψ, capturing the angular content of the diffusion propagator. Knowing that the propagator computed from equation 2.9 does not correspond to the true propagator, but to an ensemble average propagator (EAP). Fortunately, it has been demonstrated that this diffusion propagator share the same angular profile as the true propagator, thus enabling the use of the former Fourier relationship shown in 18 to establish models of the local orientation distribution functions of tissues. The ODF is thus defined as the radial integral of the diffusion propagator in spherical coordinates, This function measures the amount of diffusion in the direction of the unit vector and provides a diffusion "intensity" in every direction.

For visualisationn, ODFs can be simple as they can be complex spherical functions that cannot be visualized as ellipsoids like the diffusion tensors. The ODF is a discrete function on a sphere that can be viewed as discrete values that live on the sphere or as a more visually appealing option the radius of each vertex of the sphere can be scaled according to its corresponding value. This creates what is called glyphs that can have any shape desired as shown in fig 2.8. Hence, these glyphs are used to visualize the diffusion signal, the apparent diffusion coefficient, and the ODF, among other functions, on the sphere [21].

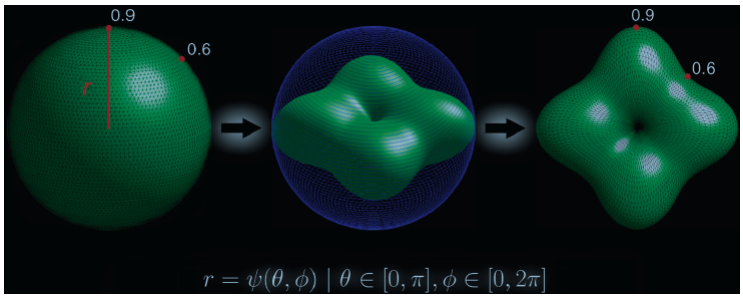

Figure 2.8: ODF visualisation by sphere and by glyph.

2.6.5 Q-ball Imaging

To reduce the time spent by DSI while probing the structure of the tissue without any modeling, a single shell HARDI technique, called q-ball was introduced [22]. Instead of sampling the whole 3D grid, suffices for q-ball technique to traverse the q-space on sphere [10] by choosing a sufficiently large diameter (b-value) so that the movement of water molecules can be captured with high precision. The number of q-values is still large but much less than DSI. this will lead a reduction of the scan time while the capability of resolving complex tissue structure is kept intact [10].
Mathematically, it has been proven that an approximation of the ODF through q-ball imaging, can be obtained simply by taking the Funk-Radon transfrom (FRT) of the spheriacally sampled q-space. If the sampled points are distributed on the surface of the sphere, then the result of FRT, the approximate value of ODF along direction that connects the south and the north poles, is the sum of all measured q-space signals on the equator [24]. Tuch showed that Funk-Radon transform reconstructs a smoothed version of the true diffusion from the single shell HARDI acquisition [23] .

2.6.5.1 Funk-Radon Transform and the Q-ball

The Funk-Radon transform assigns to a function on the two-sphere its mean values along all great circles. Hence, the Funk-Radon transform value at a particular point is the great circle integral of the signal on the sphere defined by the plane that passes through the origin and is perpendicular to the point of evaluation [18].
In general, to compute the approximate value of ODF in any direction, is to just sum all

q-space signal on the "new equator" perpendicular to the direction under consideration using the following equation :

$$G[F(w)](u) = \int \delta(u^T w) f(w) dw \tag{2.11}$$

where:
u,w are unit vectors , $f(w)$ is a function on a sphere [8].

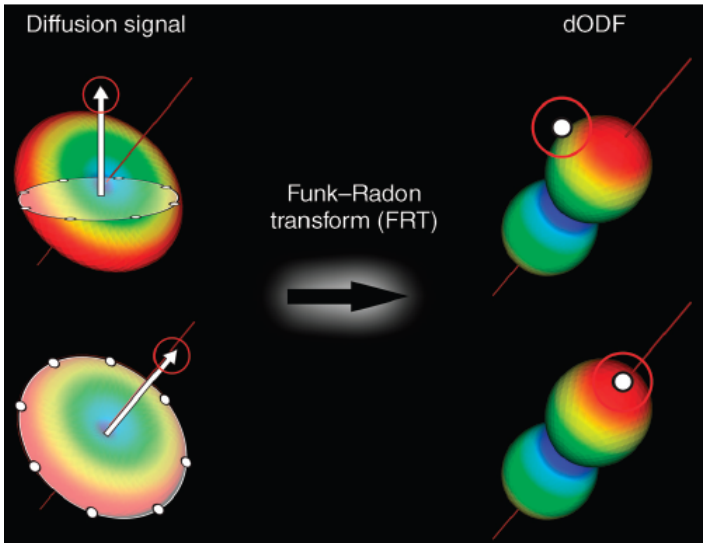

Figure 2.9: Illustration of Funk-Radon transform in the q-ball technique. Great circle integrals are computed from the measured signal to obtain the ODF.

The ODF is intuitive because it has its maximum(a) aligned with the underlying population of fiber(s). Hence, it is a more interesting function for tractography than the ADC. The original QBI has a numerical solution [22] and more recent methods [13] have introduced an analytical spherical harmonic reconstruction solution that is faster and more robust to noise.

2.6.5.2 Spherical Harmonics

Analytically, the Q-ball ODF can be obtained from the spherical harmonics (SH) which are the best mathematical tool to represent the spherical functions arising from the discrete samples on the sphere from HARDI acquisition.
Spherical harmonics transform on the shpere is equivalent to Fourier transform on the

plane [13]. Spherical harmonic of order l and phase m is denoted as $y_l^m(\theta, \phi)$ and can be computed as follow.

$$y_l^m(\theta, \phi) = \sqrt{\frac{(2l+1)(l-m)!}{4\pi(l+m)!}} p_l^m cos(\theta) e^{im\phi} \tag{2.12}$$

2.6.5.3 Modified Spherical Harmonics

As we are dealing with DMRI measaurements that represent the average attenuation of the diffusion of water molecules, the HARDI signal is assumed to be real and symmetric. Therefore, the modified SH are introduced .

In order to impose the symmetry, only the SH with even orders are considered and for the real-valued constraint, the real and imaginary parts of SH are approriatly chosen and index j is defined in terms of the order l and the degree m as shown in the equation 2.13 [9].

$$j(l, m) = \frac{l^2 + l + 2}{2} + m \tag{2.13}$$

2.6.6 Constrained Spherical Deconvolution

The idea of the spherical deconvolution emerged after noticing that any fibre population can be expressed as a linear sum of the signals of all the fibres present in a given voxel as shown in figure 2.10. This can be represented in a more general distribution of fiber orientations, and the mixture of signals becomes a spherical convulotion.

$$S(\theta, \phi) = F(\theta, \phi) \circledast R(\theta) \tag{2.14}$$

Where S is the measured signal, F is the fODF an R is the fiber response. Hence, the problem of estimating the fibre orientations themselves is solved by inverting the convolution to infer the FODF from the measured signal.

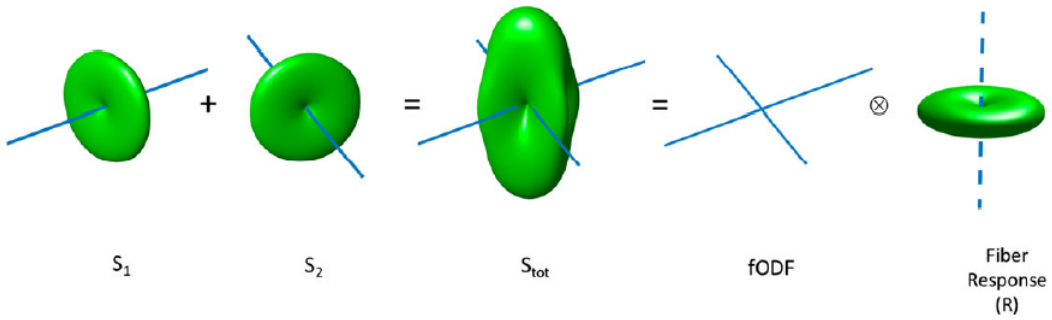

Figure 2.10: Spherical convolution approach; multiple fibre populations within a voxel contribute with additive signals (S_1,S_2) to get the total DW signal (S_{tot}) which is equivalent to the convolution of fODF with a chosen fiber response function .

The problem with the spherical deconvolution is that the resulting fODF contains negative side-lobes as shown in figure 2.11.

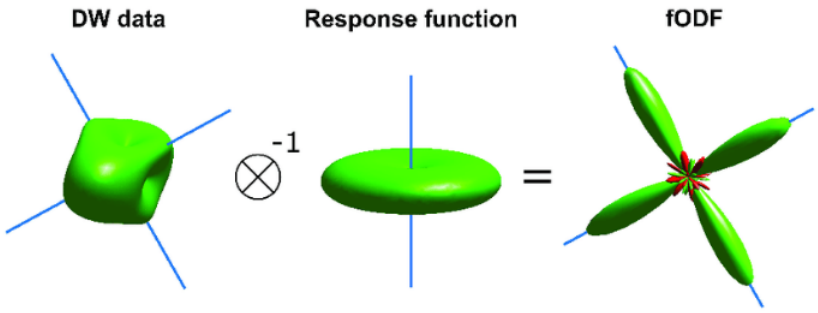

Figure 2.11: Spherical deconvolution with a maximum SH order of eight used to estimate the fiber orientation distribution function (fODF) from diffusion weighted (DW) data.

The blue lines in (fig 2.11 correspond to the actual fiber orientations,The green color corresponds to positive and red to negative values in the fODF. Because the fODF represents the distribution of fibers oriented along each direction, the negative values are not physically possible. For that reasons the constraint spherical deconvolution [21] was introduced. In the CSD approach the fODF is represented in the spherical harmonic basis, a non-negativity constraint is applied as a soft regularizer(Tikhonov algorithm).
The CSD technique procedure is summarized in the following steps :

1. Obtain the sampled data in the cartesian coordinates.

2. Transform the data into spherical coordinates.
3. Construct the matrix of SH basis.
4. Compute the coefficients of the SH for fixed order l_{max} using least square method.
5. Estimate the response function.
6. Construst the matrix of rotational harmonics.
7. Perform the deconvolution using the least squares method.
8. Find the fODFs at each voxel.
9. Eliminate negative regions using Tikhonov regularization.

2.7 Comparison of reconstruction techniques

The advantages and the disadvantages of some reconstruction techniques are summerized in Table 2.2.

Table 2.2: Advantages and disadvantages of some reconstruction techniques [23]

Technique	Voxel Information	Advantages	Disadvantages
Diffusion Tensor Imaging (DTI)	3D diffusion tensor	• Short acquisition time. • Provides information about diffusion orientation and anisotropy. • Not hardware demanding. • DTI metrics based on FA are validated and accepted. • Reproducibility studies are widely available.	• Hypothesis-based. • Does not provide accurate information of complex fiber architecture. • Tractography results are vulnerable to severe artifacts.

Diffusion Spectrum Imaging(DSI)	3D diffusion displacement distribution	• Hypothesis-free. • Provides accurate depiction of complex fiber architectures. • Maps the entire field of diffusion with possibility of many different characterizations of the imaged structures.	• Relatively long acquisition time. Recent improvements in hardware and imaging techniques have made acquisition time shorter. • Demanding hardware requirements. • Lacking consensus on proper quantitative metric. • Limited number of reproducibility studies.
Q-ball Imaging (QBI)	3D fiber orientation distribution	• Tolerable acquisition time. • Provides information about diffusion orientation and anisotropy, depiction of fiber crossings.	• Demanding hardware requirements. • Although results seem correct in important brain areas, accuracy is not guaranteed in all brain regions. Further validation of the technique required. • Lacking consensus on proper quantitative metric. • Limited number of reproducibility studies.

Table 2.3: Diffusion MRI acquisition techniques. Assuming 30 axial slice with thickness of approximately 3 mm each.

dMRI modality	gradient strength (sec/mm^2) weak	medium	straong	nbr of measurements N	time (min) fast	slow
DWI	√ ≤1000			N=1	√ 1-3	
Trace & ADC	√ ≤ 1000			$2 \leq N \leq 4$	√ 2-4	
DTI	√ ≤ 1000			N=7	√ 3-6	
Single shell HARDI		√	√	N≥60	√	√
	b≥ 1000 (b≥ 3000 desirable)				10-20	
DSI			√ b>8000	N≥200 (the more the better)		√ 15-60

2.8 Diffusion ODF vs fiber ODF

The point of divergence between the latest reconstruction techniques is wether they attempt to estimate the diffusion ODF (dODF) or instead they seek to recover the fiber ODF. Proponents of the dODF argue that it remains the most unbiased, model-free characterization of the physical process of diffusion itself. Any attempt at extracting more specific information (in particular the fODF) relies on assumptions about how the tissue microstructure influences the MRI signal. On the other hand, proponents of the fiber ODF (fODF) argue that the dODF is only providing an indirect and blurred representation of the underlying fibre orientation. Even in the presence of a single coherently oriented fibre population, dODF will provide a smooth profile, suggesting not a single sharp fibre population but rather a broad range of possible orientations centred about the main orientation.

Since the diffusion propagator is a smooth function, the computation of the dODF is inevitably penalized by an intrinsic angular blurring that limits the angular resolution or the ability to resolve two distinct fibre populations. In contrast, fODF can return a more accurate description for single or multiple fibre populations by directly deconvolving the

angular blurring introduced by the diffusion process and recovering more precisely the information of fibre orientation. For a single coherently oriented fibre population, fODF can be represented by a delta function oriented along the direction of the fibre population. In practice, however, due to regularization procedures and to account for noise instabilities and numerical errors, a smoother fODF is however always preferred[7]. Nevertheless , the recent literature shows that fODF methods consistently produce sharper functions compared to methods based on dODF [7]. Besides, the fODF has a better angular resolution than the dODF with smaller b-values.

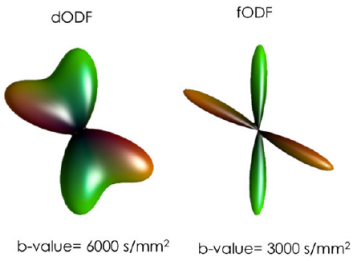

Figure 2.12: Visualisation of a 60 °fibre crossing configuration using dODF and fODF profiles. On the left, dODF is obtained from DSI, with a maximum b-value of 6000 s/mm^2. On the right, fODF is obtained using spherical deconvolution with b = 3000 s/mm^2.

2.9 Summary

One of the most challenging aspects of designing tracts is the choice of the underlying model that transform raw dMRI images to the local fibre orientations .
In this chapter, we presented several reconstruction techniques from data aquisition to the estimation of the fiber orientations Starting with DTI and its serious limitations, HARDI techniques are introduced and which are able to recover the 3D diffusion PDF and diffusion ODF of water molecules in biological tissues and recover complex multiple fiber dstribution and overcome the crossing fibres limitation .

Chapter 3

Tratography

3.1 Introduction

After the reconstruction procedure and the deduction of the fiber orientations in each voxel, we get local information. Therefore we need to integrate those local orientations to get more global information about the white matter. This is achieved by piecing all the local fiber orientatoins together to infer the long-range pathways connecting distant regions of the brain. This process is often referred to as fiber tracking or tractograpgy,. Such technique can be performed on various fibrous tissues such as cardiac muscle and skeletal muscle but its primary application has been on the central nervous system particularly the brain's white matter.

3.2 Fiber tractography

Basically, fiber tractography assumes that there exists in each imaging voxel a dominant fiber direction and connects those local orientations to infer global fiber trajectories .
Mathematically, a set of local fiber orientations can be considered as 3D vector field and global fiber trajectories as its streamlines. A streamline is any curve, that along its trajectory, is tangent to the vector field. It is parameterized by its arc length [14]. Thus for the streamline to align with vector field, its tangent at arc length has to be equal to the vector at the corresponding position :

$$\frac{dr(s)}{ds} = v[r(s)] \tag{3.1}$$

where :
$r(s)$ is the 3D position along the streamline, v is the 3D vector field.
Equation 3.1 can be solved by integrating both sides as follows :

$$r(s) = \int_{s_0} v[r(s)]ds \tag{3.2}$$

where $r(s_0)$=r_0 represents the starting point of the streamline which is considered as a seed point. The process of integrating stepwise orientations into streamlines is generally referred to as streamline tracking or tractography.

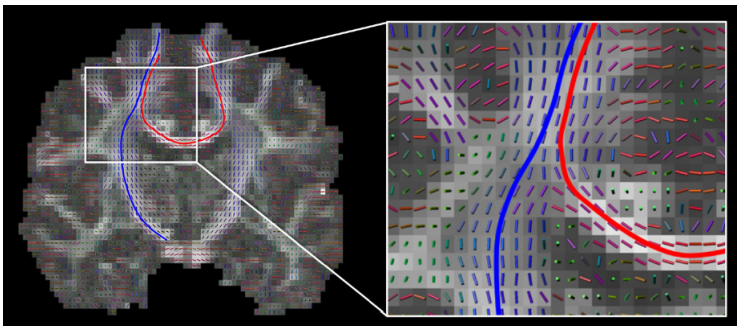

Figure 3.1: Vector field of local predominant fiber orientations and two of its streamlines depicted on a coronal view of the human brain. The blue streamline is part of the corticospinal tract, whereas the red one is part of the corpus callosum. Notice that each streamline's tangent is parallel to the local vector field [14].

3.3 Deterministic tractography

The directional anisotropic information of the diffusion tensor provides a unique apportunity for estimating and modeling the trajectories of white matter tracts in the human brain noninvasively.

Deterministic tractography methods are primarely based upon the streamline algorithms where the local tract direction is defined by the major eigenvector of the diffusion tensor. These approaches have been used to map out white matter anatomical connections in the human brain. The accuracy and and variance of the tract reconstruction depend of the algorithm, the signal-to-noise ratio, the diffusion tensor eigenvalues, and the tract length.

3.3.1 FACT and TEND algorithms

The Fiber Assignment by Continuous Tracking (FACT) algorithm is an extension to the streamline approach. It adjusts the step size depending upon the continuity of the local fibre-orientation estimates. Where adjacent fibres are well-aligned, a large step is taken; when there is no continuity between adjacent fibre-orientation estimates, a small step is taken. Such variable step size attempts to prevent the streamline from deviating from the true trajectory of the white-matter; for example, at points of high curvature or when the

streamline is close to a boundary.

More recently, Weinstein has introduced the Tensor Deflection (TEND) tractography algorithm. This algorithm uses the entire diffusion tensor to calculate the appropriate deflection, as opposed to just the principal eigenvector. Therefore, this method uses the diffusion tensor as the true PDF of the underlying fibre distributions. In voxels where the anisotropy is high, the streamline follows the principal eigenvector of the diffusion tensor. However, as the diffusion tensor becomes more isotropic, the path of the streamline is deflected less [19].

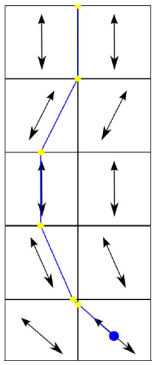

Figure 3.2: Fiber assignment by continuous tracking algorithm starting from the bleu point(seed point).

The FACT algorithm is summarized in the flowchart below.

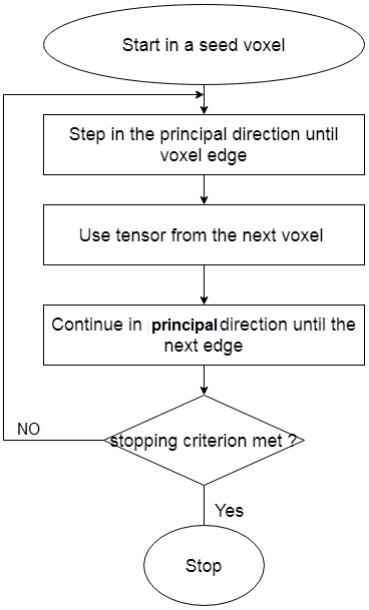

Figure 3.3: Fiber assignment by continuous tracking algorithm .

3.3.2 Streamlines integration

MR diffusion tractography is a method to identify white matter pathways in the living human brain. These pathways form the substrate for information transfer between remote brain regions and are therefore central to our understanding of function in both normal and diseaded brain.

A stramline through a vector field is any line whose tangent is always parallel to the vector field. Such streamlines are the intuitive method for performing tractography as they can be reconstructed by simply starting at a seed point and following the local vector information on a step-by-step basis, effectively "joining the arrows" [16].

Mathematically, a streamline can be represented by equation 3.1 and to perform that integration numerous numerical methods can be used. The most commonly used methods are the Euler method and the Runge-Kutta method. Those are briefly explained in the subsequent sections.

3.3.2.1 Euler method

The idea behind Euler's integration is that "very" locally, the solution is "approximately" linear, it follows the current flow vector $v(r)$ from the current streamline point r_i for a very small time (dt) and therefore distance [15].

$$s_{i+1} = s_i + v(r_i)dt \tag{3.3}$$

Euler's algorithm is presented in the following pseudocode.

Algorithm : Euler's algorithm

```
Select the nbr of steps N;
k = K − 1 ;
set dt = r_k r_0 / N;
while K ≥ 0 do
    r_{k+1} = r_k + dtv(r_k;
end
```

Table 3.1: Error table of the above Euler's integration example with different step sizes.

dt	nbr of steps	error
1/2	19	$\sim 200\%$
1/4	36	$\sim 75\%$
1/10	89	$\sim 25\%$
1/100	889	$\sim 2\%$
1/1000	8889	$\sim 0.2\%$

The Euler's method is generally used beacause it is simple and direct. However, it is less accurate and numerically unstable. In addition, the approximation error is proportional to the step size h, hence a good approximation is obtained with a very small h. This requires a denser of discretization leading to a longer computation time [12].

3.3.2.2 Runge Kutta

In order to take into consideration the variations of v between r_i and r_{i+1} so that the errors will be reduced, Runge-Kutta method is used. The idea behind it, is to cut short the curve arc .
RK2(second order Runge Kutta)algorithm consists of the following steps [3]:

1. Do half a Euler step .
2. Evalute flow vector there.
3. Use it in the origin.

A still better method is the fourth order Runge-Kutta which gives better precision but with more computations.

Algorithm : Runge Kutta's algorithm

$K_1 = v(r_i);$
$K_2 = v(r_i + \frac{K_1}{2});$
$K_3 = v(r_i + \frac{K_2}{2});$
$K_4 = v(r_i + K_3);$
$r_{i+1} = r_i + \frac{K_1+2K_2+2K3+K_4}{6}$;

It is true that Runge-Kutta has a good precision and it is easy to implement ease of implementation but it requires relatively large computer time and the erroris not easy to be estimated.

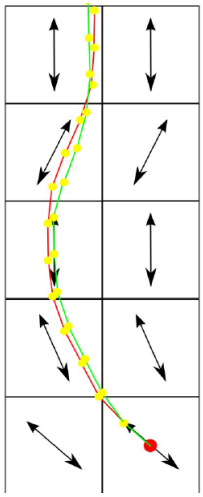

Figure 3.4: FACT algorithm using Euler's method (red) Runge-Kutta method(green).

3.4 Interpolation

The integration process requires that the local fiber orientations be available at arbitrary positions in space, which do not necessary align with the regular grid of acquired voxel positions. Therefore, a method for interpolating the discrete measurements into continuous space is needed. The simplest method to obtain an estimate of the local fiber orientation at any local fiber is to use the nearest-neighbor interpolation. This method approximates the desired fiber orientation by that of the nearest voxel. However, this approach leads to considerably greater interpolation errors than approaches that perform a smooth interpolation between grid points.

Smooth interpolation methods assume that the fiber orientations between grid points contain contributions from each neighboring point. Most algorithms use trilinear interpolation, where the local fiber orientations are calculated as a weighted sum from the eight voxels nearest to the point of interest, with the weight of each neighboring voxel determined by its distance from the point of interest.

Some implementations perform trilinear interpolation on the raw-diffusion weighted data and recompute the local fiber orientations based on the interpolated data. Another ap-

proach is to directly interpolate the local fiber orientation information.

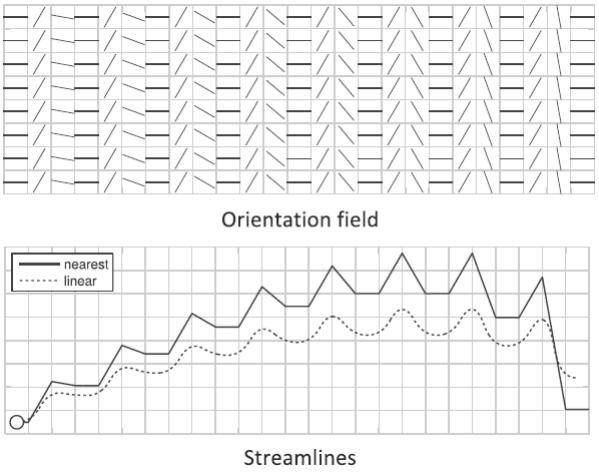

Figure 3.5: Nearest-neighbor versus smooth (linear) interpolation. The seed point is indicated as a white dot. Note that, as we move away from the seed point, the errors made by the nearest-neighbor interpolation accumulate [14].

3.5 Seed point selection

The idea about the seed point selection is that the streamlines should not get too near to each other, the approach is to choose a seed point with distance d_{sep} from an existing streamline then backward and forward-integration until distance d_{test} is reached (fig 23. d_{sep} is the separating distance given by the user and represents the minimal distance between seed points and streamlines and d_{test} is a percentage of d_{sep} (see fig 24 the effect of changing the percentage) and corresponds to the minimal distance under which the integration of the streamline will be stopped in the current direction [6].
The seed point selection is made according the following pseudocode:

Algorithm : How to select seed points

```
Finished=False;
while !Finished do
    str=str[i];
    get new seed point which is away from the current streamline;
    if Successful then
        Compute new streamline and add it to the queue ;
    else if no more stramlines in the queue then
        Finished=True ;
    else
        i++
    end ;
end
```

3.6 Track termination

White matter pathways terminate in the grey matter where the orientations uncertainty is very high. Stopping criteria usually ensure that the streamline does not leave the brain or turn back in itself. Also entering the grey matter may be a reason to stop tracking which can be detected when the fractional anisotropy falls below a threshold value . Another stopping criterion is the curvature threshold that imposes maximum local curvature of the tracks. As it is unusual to find bends in white matter bundles, then if the angle between two succesive steps is above the threshold, the track is terminated .

Besides the termination criteria, fiber tracking algorithms also uses acceptance /rejection criteria. The widely used criterion is that of minimal track length, rejecting short, often spurious, tracks. More advanced stopping criteria are based on anatomical priors, and reject tracks that terminate in cerebrospinal fluid or within white matter and only accept tracks that connect different gray matter regions. Some of the condition that can cause the track to stop are listed below.

- distance to neighboring streamline $\leq d_{test}$.
- Streamline leaves flow domain.
- Streamline runs into fixed point ($v = 0$).

- streamline gets too near to itself.
- After a certain amount of maximal steps.

3.7 Probabilistic tractography

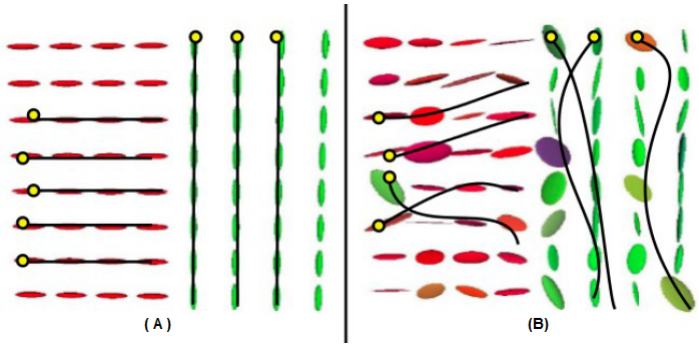

Figure 3.6: Fiber distribution A)ideal B)real .

The main problem with the deterministic tractography methods, as the one shown in figure 3.6, is the lack of information they provide regarding the error in the tracking procedure in any given experiment. Without such knowledge, it is not possible to know how much confidence we should have in the observed results. Probabilistic tractography methods attempt to overcome this limitation by explicit characterization of the confidence with which connections may be established through the diffusion MRI data set [4] .

While deterministic tractography algorithms assume a unique fiber orientation estimate in each voxel, such that a single pathway emanates from each seed point, probabilistic tractography methods generate a large collection or distribution of possible trajectories from each seed point (see figure 20, Then, the paths with higher densities of the resulting trajectories are deemed to be the right ones and then be connected to the corresponding points.

To extend probabilistic tractography algorithms to exploit multiple fiber directions requires one additional piece of information which is a model of the uncertainty of each fiber-orientation estimate.

Parke, Alexander and Cook, generalize calibrated probabilistic index of connectivity (PICo) to use multiple tensor and improve tracking through fiber crossing. As with the original implementation, the FA of each tensor predicts the uncertainty ODF as shown in figure 3.7.

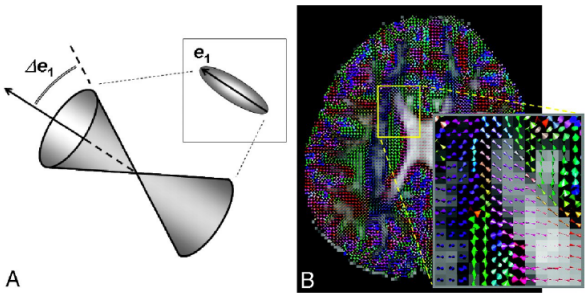

Figure 3.7: Visualisation of uODF A)zoomed in voxel B) An example of the double-cone map showing the fiber direction and its uncertainty simultaneously.

Errors in the estimation of fiber orientation can be graphically depicted on a voxel-by-voxel basis by using, for example, the double-cone diagram figure3.7, in which the principal eigenvector of a diffusion tensor ellipsoid in an image voxel replaced by a double-cone, whose angular width represents the data-fitting uncertainty.

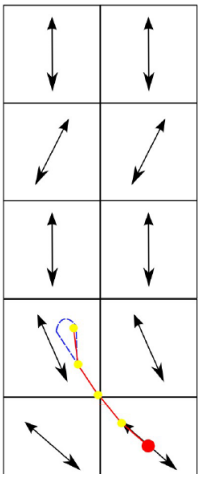

Figure 3.8: Tracking using the probabilistic algorithm.

Probabilistic method consists of steps summarized in the following flowchart.

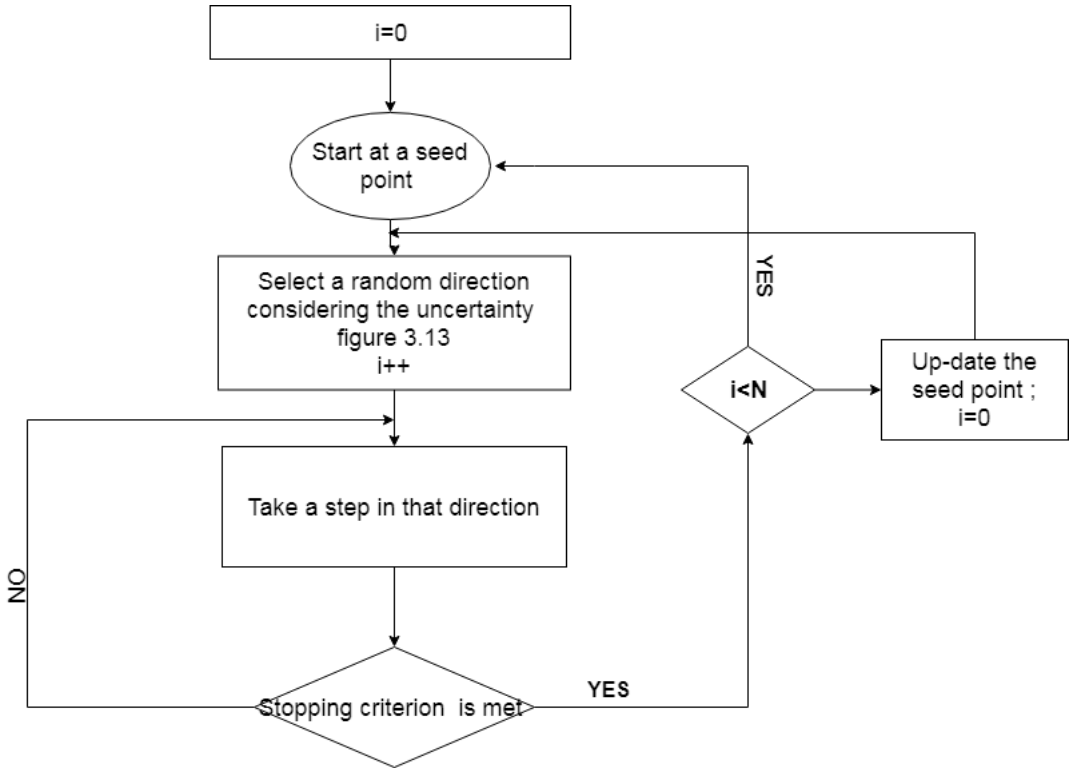

Figure 3.9: Flowchart of the probabilistic method.

The results from the flowchart (figure 3.9) are shown in (figure 3.10) .

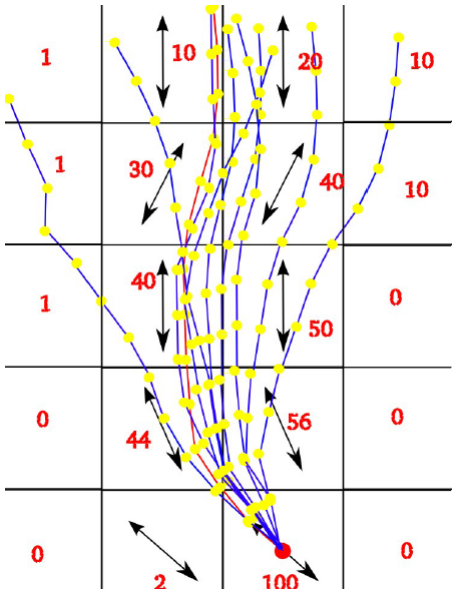

Figure 3.10: All possible paths using the probabilistic tractography.

3.7.1 Bootstrap

The bootstrap technique creates a large number of samples from a smaller dataset to improve the estimates of statistics. The standard method requires multiple acquisitions of the signal for each measurement. To create a new sample, one of each of the measurements is drawn at random from the set of repeats to provide a new combination[19] .

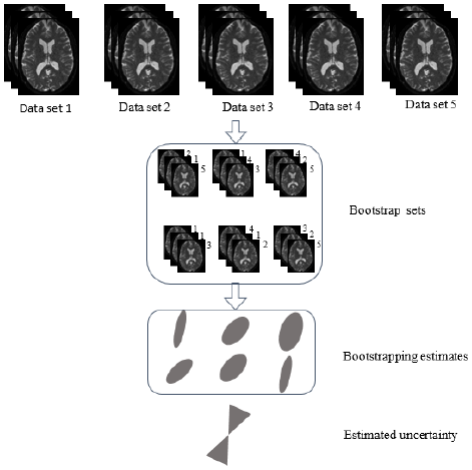

Figure 3.11: Bootstrap technique illustration.

3.8 Probabilistic vs deterministic

After studing both deterministic and probabilistic tractography methods. We can state some differences conserning the two techniques. Their advantages and disadvantages are shown in table 3.2.

Table 3.2: Advantages and disadvantages of probabilistic and deterministic tractography.

	deterministic	probabilistic
Advantages	Fast simple Reliable	Deal with crossing fibers Robust to noise
Disadvantages	Crossing fibers sensitive to noise	Burden computation → time consuming

3.9 Summary

In this chapter we viewed tractography with its two sorts probabilistic and deterministic, their algorithm such as (FACT and Tend) and how the probabilistic defines the right path from tens of resulting paths, we also talked about the advantaged and disadvantages of each method and some numerical techniques for integration of small orientations to generate the trajectories and interpolation between two voxels.

Chapter 4

Experimental part

4.1 Introduction

The objective of this chapter is to obtain the best reconstruction of abnormal tissues in the brain (WM) to assist surgeons for a better intervention. For that, we will use both the probabilistic and deterministic algorithms and varying the stopping criteria then analyze the results from the medical point of view.

4.2 Software environment

4.2.1 Dipy

Diffusion Imaging in Python (Dipy) is a free and open source software project for the analysis of data from diffusion magnetic resonance imaging(dMRI) experiments. dMRI is an application of MRI that can be used to measure structural features of brain white matter. Many methods have been developed to use dMRI data to model the local configuration of white matter nerve fiber bundles and infer the trajectory of bundles connecting different parts of the brain. Dipy gathers implementations of many different methods in dMRI, including:diffusion signal pre-processing; reconstruction of diffusion distributions in individual voxels; fiber tractography and fiber track post-processing, analysis and visualization.

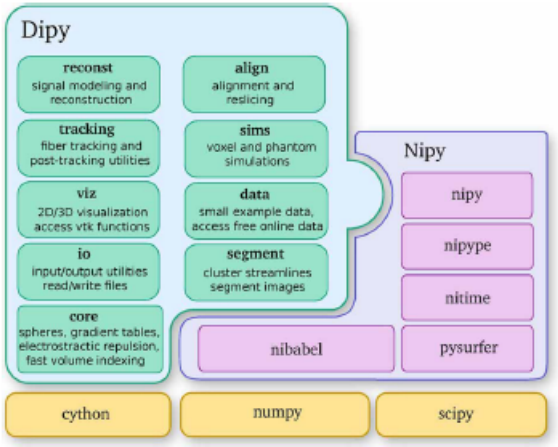

Figure 4.1: Major dipy sub-modules and its relation to Nipy, Numpy, Scipy and Cython community.

4.2.2 Mango

Multi-image Analysis GUI (Mango) is a viewer for medical search images. It provides analysis tools and a user interface to navigate image volumes.

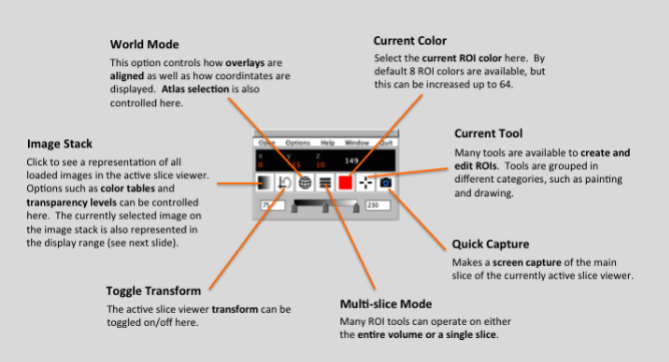

Figure 4.2: Toolbox buttons of Mango.

4.2.3 MRi-brain

MI-Brain is built on top of the MITK library, which is also based on the VTK and ITK libraries. This enables the software to support various types of neuroimaging datasets and support a wide range of file formats. 2D, 3D and 4D images, regions of interest (ROIs), tractograms and surfaces are loaded and saved from the application. One major difference with other visualization tools, such as TrackVis, BrainVisa, ExploreDTI or FiberNavigator, is that all data types can be loaded simultaneously in a common space using the 3D transformation information contained in the header of each loaded file, even if they don't have the same dimensions, voxel size .

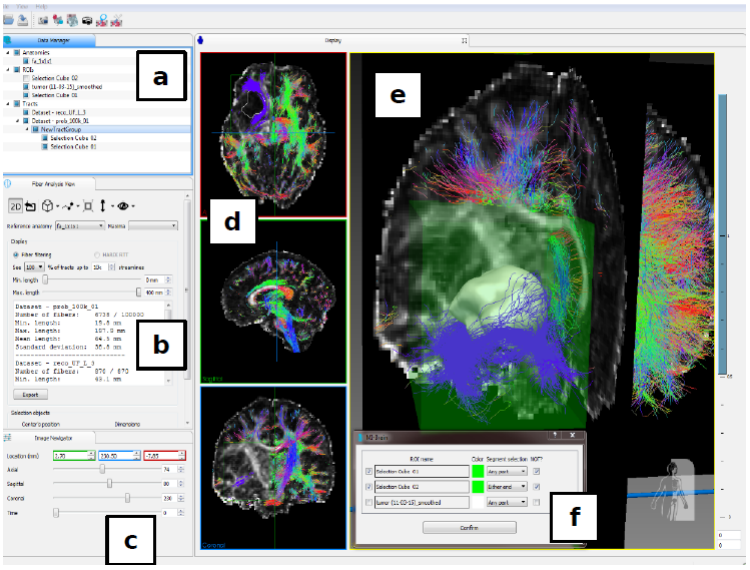

Figure 4.3: A standard view of MI-Brain.

Many pluging setups are available or can be moved and resized. a) the DataManager plugin displays all loaded datasets. b) the FiberAnalysis plugin displays streamlines' statistics and buttons for various dissection and coloring options. c) the ImageNavigator plugin navigates through 3D slices or the 4th dimension (DWI for example). d) 3 planar slices with intersecting streamlines. e) 3D view showing loaded datasets. f) popup for segmentation criteria to select options for streamlines' selection using ROIs.

4.2.4 Dcm2nii(MRIcron)

Dcm2nii is a popular tool for converting images from the complicated formats used by scanner manufacturers (DICOM, PAR/REC) to the simple NIfTI format used by many scientific tools. Dcm2nii works for all image modalities (CT, MRI, PET, SPECT) and sequence types and it has traditionally been included with MRIcron downloads.

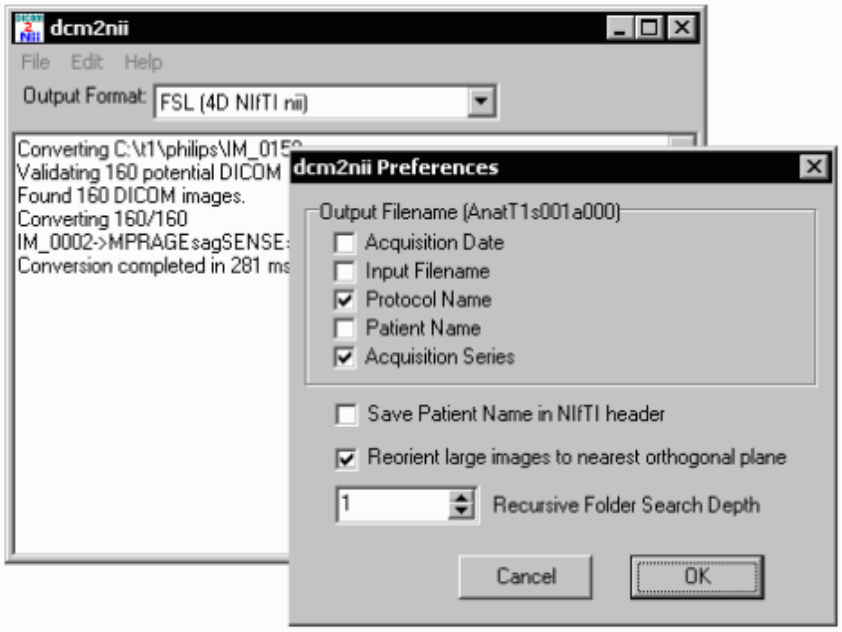

Figure 4.4: Dcm2nii tool box.

4.3 Dataset

For this study we downloaded data from the UK data service (http://ukdataservice.ac.uk/) under collection name: 'A neuroimaging dataset of brain tumour patients' which were acquired on a GE Signal HDxt 1.5 Tesla scanner with an 8 channel phased-array head coil at the Brain Research Imaging Centre, University of Edinburgh, UK.
The data MRI's parameters are summarized in table 4.1.

Table 4.1: Summary of Data's MRI parameters.

Sequence	T1	T2	DWI
Pulse type	3D IRP (inversion recovery prepared)	FAST spinecho	single-shot spin-echo EPI
In plane FOV	256 × 256mm		
In plane matrix	256 × 256		128 × 128
Slice thickness	1.3mm		2mm
Number of slices	156	72	
Acquisition order	front to back	top to bottom	
TR	10 s	2.5 s	16.5 s
TE	4 s	102 ms	98 ms
Nb of volumes in the time series and	1	1	71 (7 × b=0 64 × b=1,000 s / mm^2)

4.3.1 Data pre-processing

Clinical imaging data are typically stored and transferred in the Digital Imaging and Communications in Medicine (DICOM) format, whereas the Neuroimaging Informatics Technology Initiative (NIfTI) format has been widely adopted by scientists in the neuroimaging community. Therefore, a vital initial step in processing the data is to convert images from the complicated DICOM format to the much simpler NIfTI format.

In our case, we used the dcm2nii application provided in the MRIcron software, then we used Matlab to compress the files to a 4D file with .nii.gz extension which will be processed latter by Dipy.

4.3.2 Data loading

The experiment is started by loading the data and providing their paths.
The data to load consists of the following:

- 4D Nifti file.
- b-value file.
- b-vector file.

This is done using the following instructions:

```
from os.path import expanduser, join
home = expanduser('~')
dname = join(home, '.dipy') # Path to the data being processed
fdwi = join(dname, 'myfile21.nii.gz')
fbval = join(dname, 'bl.bval')
fbvec = join(dname, 'bv.bvec')

import nibabel as nib
img = nib.load(fdwi)
affine = img.affine
data = img.get_data()
print('data shape', data.shape)
print(img.header.get_zooms()[:3])

from dipy.io import read_bvals_bvecs
bvl, bvc = read_bvals_bvecs(fbval, fbvec)
from dipy.core.gradients import gradient_table
gtab = gradient_table(bvl, bvc)
```

After loading the data it is denoised by removing the background and extract the brain only using the median-otsu mask as follow.

4.3.3 Data processing

After loading the data and removing the background, the reconstruction step is undertaken. In our experiment we use the constrained spherical deconvolution (CSD) is used to overcome the crossing fiber limitation.
This method is mainly useful with datasets with gradient directions acquired on a spherical grid.

The basic idea with this method is that if we could estimate the response function of a single fiber then we could deconvolve the measured signal and obtain the underlying fiber distribution.
In CSD there is an important pre-processing step: the estimation of the fiber response function. In order to do this we look for regions of the brain where it is known that there are single coherent fiber populations. For example if we use an ROI at the center of the brain, we will find single fibers from the corpus callosum. The auto-response function will calculate FA for an ROI of radius equal to roi-radius in the center of the volume and return the response function estimated in that region for the voxels with FA higher than 0.7.
We use fractional anisotropy (FA) as a stopping criteria and the easiest way to generate the FA for each voxel in the brain we can use the DTI-reconstruction as follow.

```
tensor_model = TensorModel(gtab, fit_method='WLS')
tensor_fit = tensor_model.fit(data, mask)


fa = tensor_fit.fa
```

Then we compute the response using the following instructions.

```
response, ratio = auto_response(gtab, data, roi_radius=10, fa_thr=0.7)
```

After getting the response, we are ready to start the deconvolution process and get the model.

```
csd_model = ConstrainedSphericalDeconvModel(gtab, response)
```

The next step is to extract the peaks(maxima of the ODFs) to deduce the fiber directions sor that we use **peaks_ from_ model**.

```
csd_peaks = peaks_from_model(model=csd_model,
                             data=data,
                             sphere=sphere,
                             mask=mask,
                             relative_peak_threshold=.5,
                             min_separation_angle=25,
                             parallel=False)
```

After collecting the peaks we choose either the probabilistic and the deterministic and we set the stopping criteria.

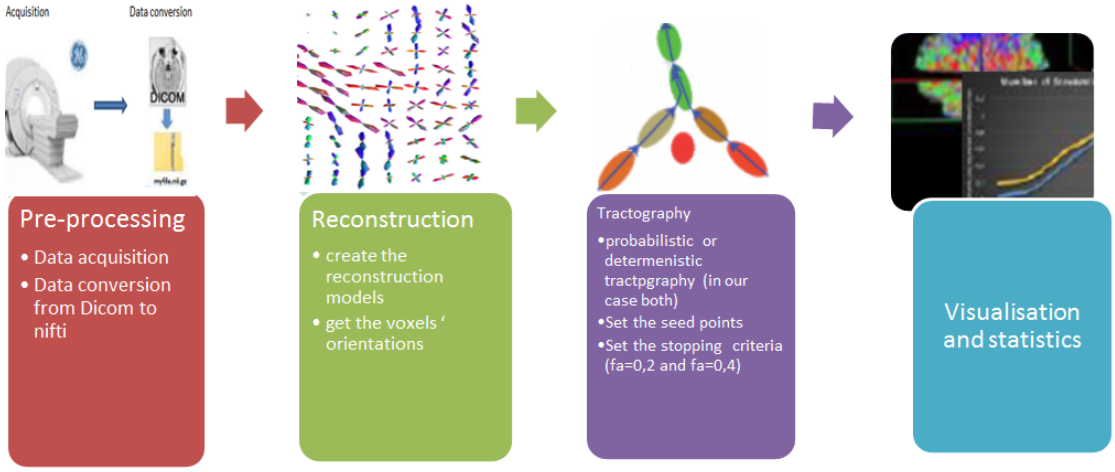

Figure 4.5: The required steps to perform the tractography study. 1)Data acquistion and conversion. 2)data reconstruction. 3)tractography. 4)visualisation and statistics.

4.4 Comparison of tractography algorithms

For our study, we used nine patients from the UK dataset archive, their clinical information are summarized in the table 4.2.

Table 4.2: Summary of the clinical data used in the study.

	Pathology	tumour location	Volumes (litre)				Sex	Age
			GM	WM	Tunour	CSF		
1	Oligodendrocytoma type II	Left Supplementory Motor Area	0,580105	0,5237809	0,03191445	0,2922474	M	43
2	Astrocytoma type III	Right Supplementory Motor Area	0,5834562	0,3857222	0,05487587	0,1544075	F	25
3	Astrocytoma type II	Left temporal cortex	0,613226	0,53236	0,09157683	0,1708056	F	27
4	Glioblastoma Multiform	Right primary motor area	0,6016713	0,4441813	0,1124203	0,2053155	F	40
5	Astrocytoma type II	Wernicke area	0,6495395	0,4648716	0,02123101	0,3508827	M	41
6	Meningioma type II	Left primary motor area	0,5607807	0,4023127	0,1041229	0,2644679	M	68
7	Glioblastoma Multiform	Left Supplementory Motor Area	0,609486	0,5608176	0,03046183	0,2345833	M	30
8	Meningioma	Left Pre-Motor area	0,5649637	0,4794921	0,1649987	0,2876655	M	54
9	Glioblastoma Multiform	Right primary motor area	0,6703304	0,5900926	0,05628418	0,2827172	M	42

The flowchart below describes the followed steps to obtain the results we will analyze latter.

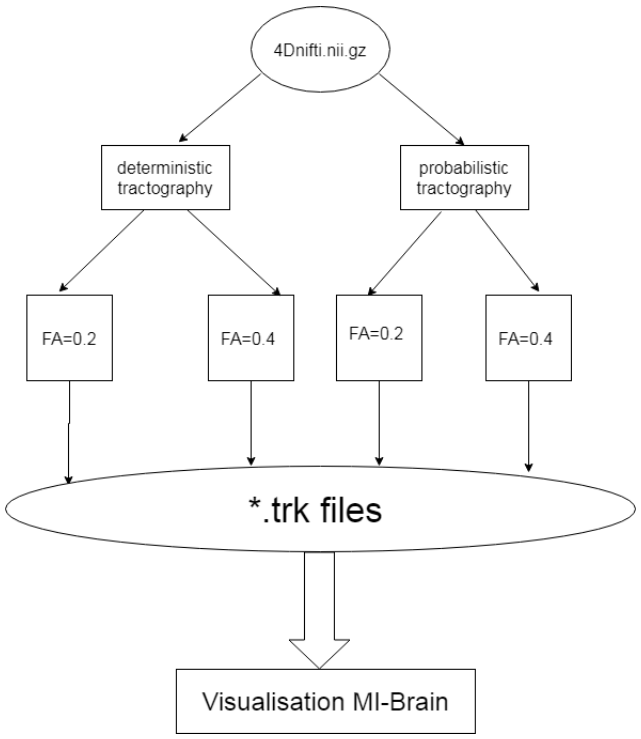

Figure 4.6: Flowchart resuming the needed files for the study.

To better locate the region affected by the tumor, we use mango (Nifti viewer). The results are in the figure 4.7.

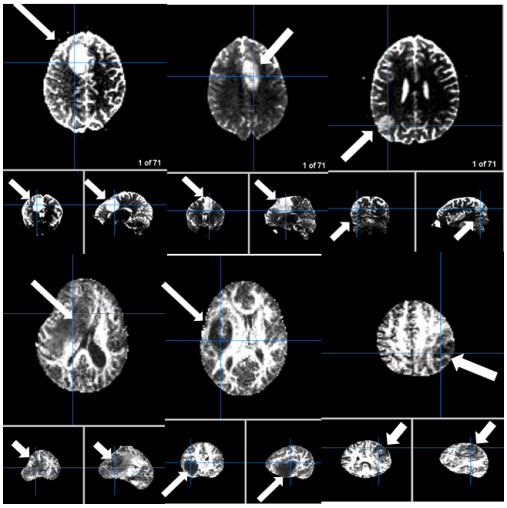

Figure 4.7: some results for visualising nifti with mango.

4.5 Analysis and discussion

After the .trk files are collected, MI-brain for 3D view is used (figure 4.8).

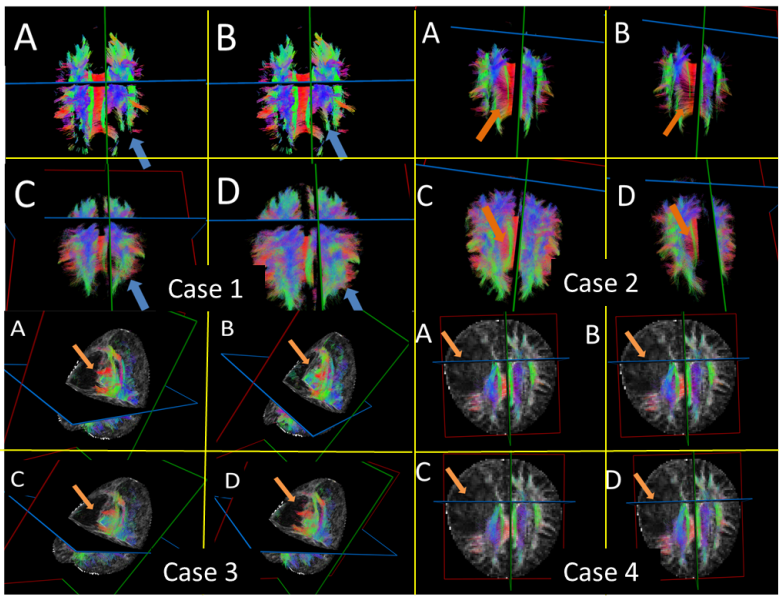

Figure 4.8: Resulting tract using different parameters. A) deterministic algorithm with FA=0.4, B) deterministic algorithm with FA=0.2, C) probabilistic algorithm with FA=0.4, D) probabilistic algorithm with FA=0.2.

All four cases in figure 4.8 show a difference between A,B and C,D tracts. All of them ensure the existence of abnormalities in the tissue but C and D give a more complex and realistic reconstruction that help surgeons to intervene in the most efficient way.
The total number of streamlines generated by the deterministic and probabilistic methods are shown in table 4.3.

Table 4.3: Total number of streamlines generated from deterministic and probabilistic methods.

	Deterministic		Probabilistic	
	FA=0.4	FA=0.2	FA=0.4	FA=0.2
Case1	52926	179678	31014	91777
Case2	45107	151905	24948	51359
Case3	66357	219447	37702	108197
Case4	36408	146796	23564	82337

Discussion

From table 4.3, we notice that the number of streamlines generated using FA=0.2 is greater than using FA=0.4 this is because more seeds were placed for tractography using FA=0.2 then FA=0.4. Tracking with FA=0.4 is to track in a very restricted WM mask, also probably removing part of crossing area where the FA is low due to the crossing. Generally, FA will be set to lower value (e.g. 0.1) in the presence of tumor to allow tracking through the edema area, where the FA is typically lower than healthy WM. The comparison between deterministic and probabilistic is interesting, especially at FA=0.2. Another remark is that when using the same FA, the deterministic algorithm generates more streamlines. This due to the fact that the probabilistic method connects more voxels which results in less but longer streamlines. This hypothesis is proved by using an option in MI-brain where we could compute the longest streamline generated then filter the streamlines according to their lengths. The results are summarized in tables 4.5 and 4.5.

Table 4.4: the maximum length generated from each method (the colored cells corresponds to the largest length for the same patients).

Case	Deterministic		Probabilistic	
	FA=0,2	FA=0,4	FA=0,2	FA=0,4
1	82,5	97,5	188,5	185,5
2	114,8	102,8	147	168
3	122,3	120,5	131,4	125,4
4	128,2	103,5	128	125,1
5	124,8	123,3	193	125,5
6	124,1	121	125	120
7	129,3	76,5	111	118,4
8	102,5	131,1	133,6	134
9	181,5	234,1	172,1	253,4

Table 4.5: Number of streamlines after setting the min_ length to 90 mm except for case 9.

Case	Deterministic		Probabilistic	
	FA=0,2	FA=0,4	FA=0,2	FA=0,4
1	0	3	922	558
2	13	2	300	170
3	3	8	20	12
4	23	1	30	8
5	56	18	90	34
6	34	52	38	11
7	8	0	6	14
8	4	19	84	13
9(min=170mm)	9	3	3	9

The two exceptions in table 4.5 case 4 and 5 can be explained by zooming in the generated tracts. The difference is shown in the figure 4.9.

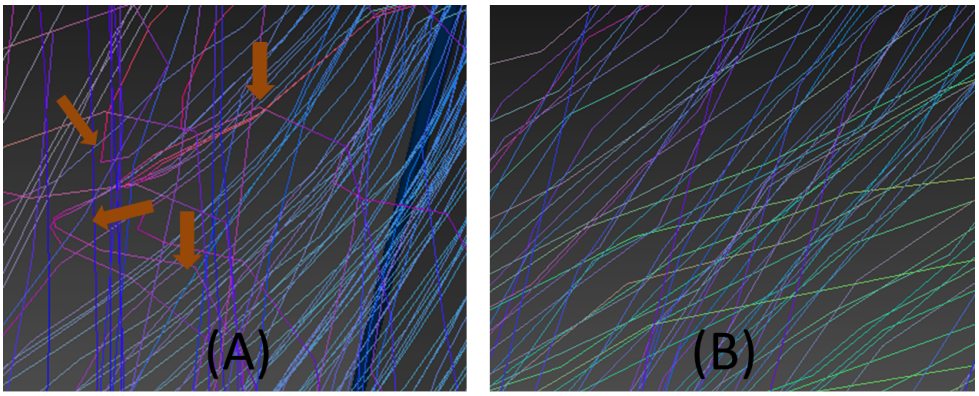

Figure 4.9: Voxel-wise assessment of deterministic and probabilistic tractography. Isolated voxel depicting the streamlines passing through it. A) the fibers generated with deterministic tractography shows acute bends. B) fibers generated with probabilistic tractography shows smoothness

From figure 4.9, we notice in (A) acute bends that do not exist in the brain, unlike (B) where the streamlines are smooth because of the conditions that must be fullfilled before doing any connection between two voxels including setting the min_ angle to avoid such acute angles something that makes the reconstruction, using the probabilistic method closer to the real architecture of the WM. Therefore we can state that the fibers generated from deterministic method in cases 4 and 5 are not necessarily existing fibers.

Comparing right and left hemispheres

The tables 4.6, 4.7, 4.5 and 4.5 show for the four first cases, the number of streamline in the left and the right hemispheres. The colored cells correspond to the damaged one.

Table 4.6: Number of streamlines in the right and the left hemispheres case1.

Nbr of streamlines	Deterministic algorithm		Probabilistic algorithm	
	FA=0,4	FA=0,2	FA=0,4	FA=0,2
right hemisphere	27983	93821	14493	44140
left hemisphere	22262	82877	10971	37115
Corpus collusum	2681	3824	5575	10675

Table 4.7: Number of streamlines in the right and the left hemispheres case2.

Nbr of streamlines	Deterministic algorithm		Probabilistic algorithm	
	FA=0,4	FA=0,2	FA=0,4	FA=0,2
right hemisphere	20815	76331	9884	32604
left hemisphere	21488	70870	9945	29833
Corpus collusum	2811	9230	5119	10072

Table 4.8: Number of streamlines in the right and the left hemispheres case3.

Nbr of streamlines	Deterministic algorithm		Probabilistic algorithm	
	FA=0,4	FA=0,2	FA=0,4	FA=0,2
right hemisphere	33344	107191	18507	51359
left hemisphere	29895	108700	16752	53564
Corpus collusum	3423	5063	2482	3514

Table 4.9: Number of streamlines in the right and the left hemispheres case4.

Nbr of streamlines	Deterministic algorithm		Probabilistic algorithm	
	FA=0,4	FA=0,2	FA=0,4	FA=0,2
right hemisphere	17056	107191	10796	51359
left hemisphere	29895	108700	11520	53564
Corpus collusum	3423	5063	2482	3514

From tables 4.6 and 4.5, we notice that the number of streamlines in the damaged hemisphere is less than the non-damaged one and this is due to the tumor's effect in damaging fibers so the diffusivity reduces. Therefore less fibers are detected while in table 4.7 and 4.5; using FA=0.2, there are more streamlines in the damaged hemisphere. The possible reason for this is that the tumor destructs the fibers, so that the number of the affected fibers will double as they are cut.

Comparing the performance of the same algorithms in ROI

After visualizing and analysing the performance of the algorithms in the whole brain, the ROI is extractes to be studied it separately using the segmentation tool. The results of the four cases are shown in figures 4.10, 4.11, 4.12 and 4.13.

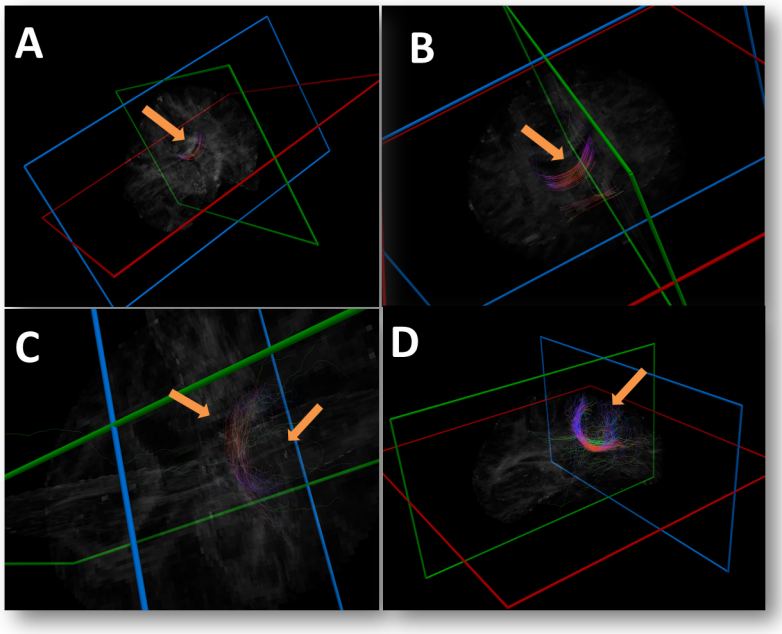

Figure 4.10: Tracts behavior inside the tumor region(ROI) case1. A) tract using DFA=0.4, B) tract using DFA=0.2, C) tract using PFA=0.4, D) tract using PFA=0.2.

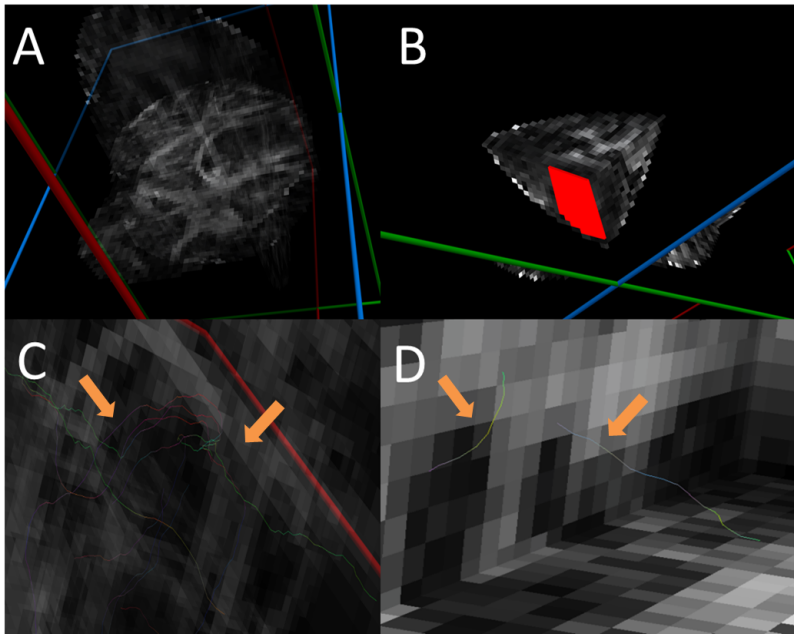

Figure 4.11: Tracts behavior inside the tumor region(ROI) case2. A)tract using DFA=0.4, B)tract using DFA=0.2, C)tract using PFA=0.4, D)tract using PFA=0.2.

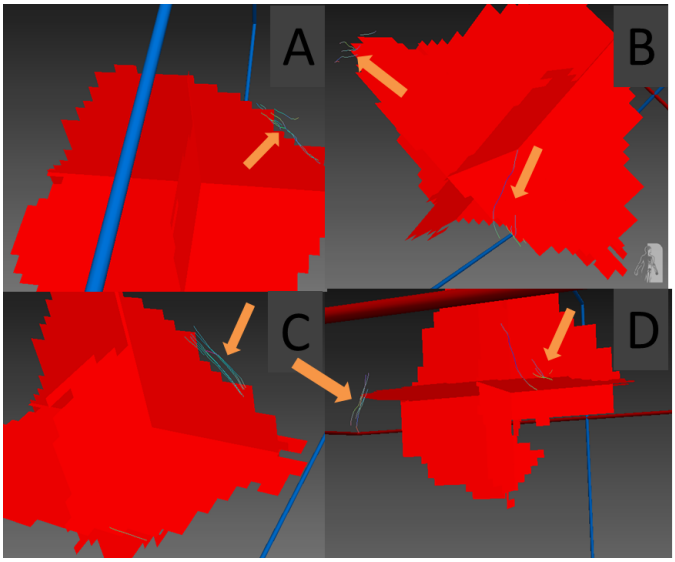

Figure 4.12: Tracts behavior inside the tumor region(ROI) case3. A) tract using DFA=0.4, B) tract using DFA=0.2, C) tract using PFA=0.4, D) tract using PFA=0.2.

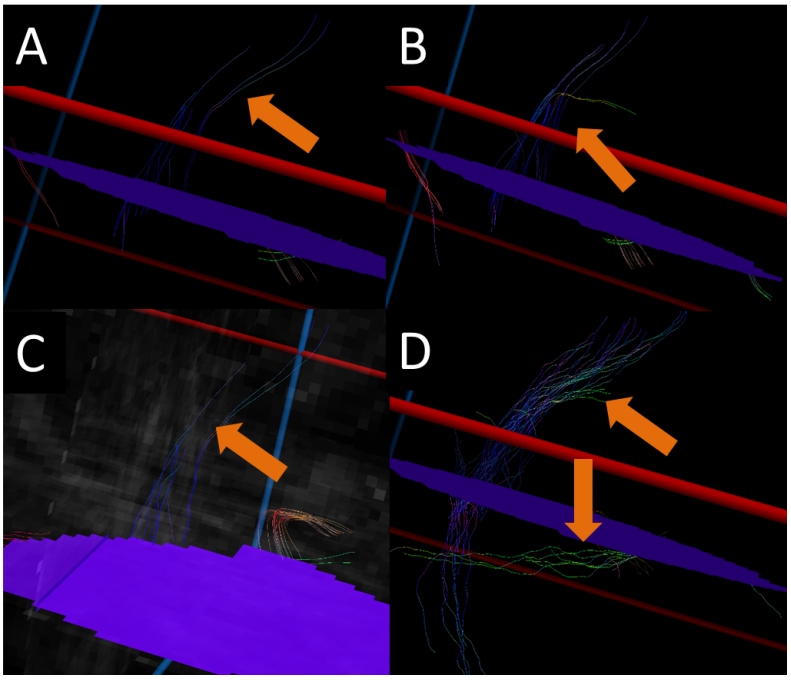

Figure 4.13: Tracts behavior inside the tumor region(ROI) case4. A) tract using DFA=0.4, B) tract using DFA=0.2, C) tract using PFA=0.4, D) tract using PFA=0.2.

The number of fibers in the ROI from the four tracts are represented by the histogram in figure 4.14.

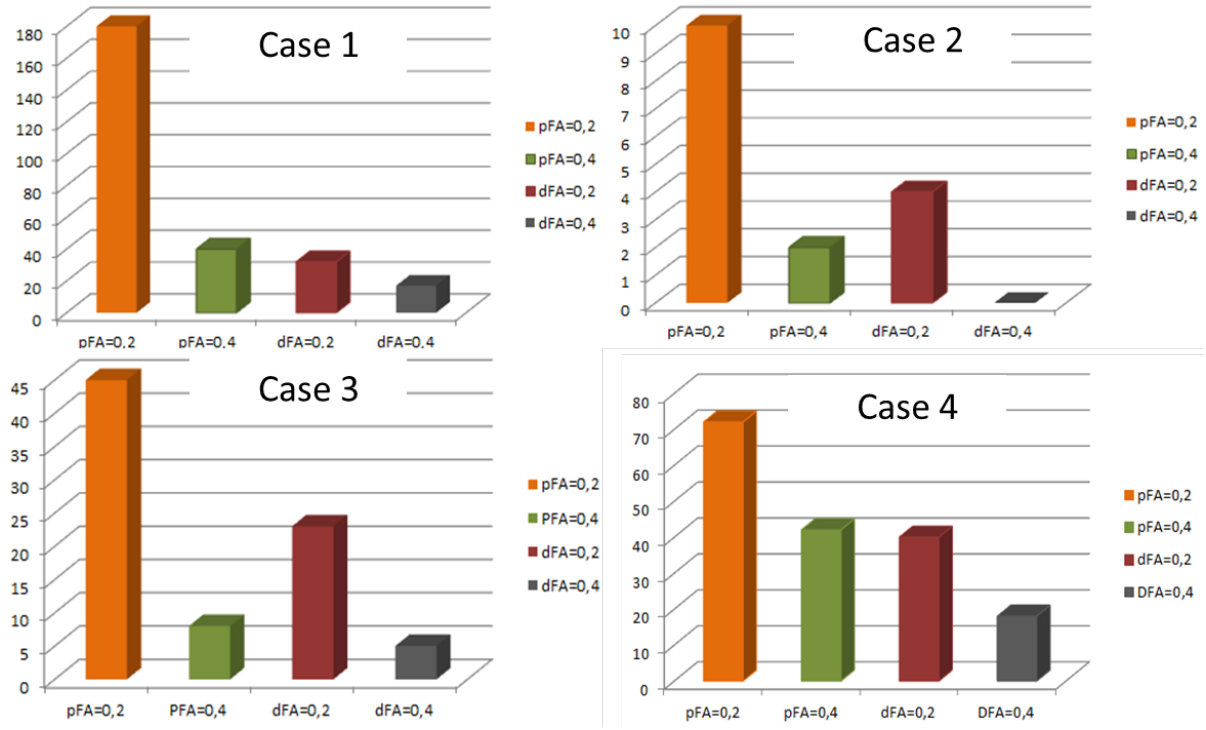

Figure 4.14: Number of fibers in ROI for the four cases; DFA=0.2 and DFA=0.4 are for tracts using deterministic algorithm with stopping criterion FA=0.2 and FA=0.4, respectively. PFA=0.2 and PFA=0.4 are for tracts using probabilistic algorithm with stopping criterian FA=0.2 and FA=0.4, respectively.

From figures 4.10, 4.11, 4.12, 4.13 and histograms shown in figure 4.14, we notice that the probabilistic method gives better results than the deterministic method; specially when using FA=0.2 which allows the detection of more fibers. In figure 4.10, we notice that the tract enters inside the ROI and this explains the existence of an edema while in other cases the tracts enter slightly to the tumor and that is because the tumor destructs the fibers in the ROI.
From those results we conclude that the tumor affects the brain in different ways.

The results of the remaining cases ensure our conclusions and shown in the tables below:

Table 4.10: The total number of the streamlines generating from deterministic and probabilistic for cases 5, 6, 7, 8, 9.

Case	Deterministic		Probabilistic	
	FA=0,2	FA=0,4	FA=0,2	FA=0,4
5	154897	45574	83259	27690
6	126239	30638	70433	19185
7	176355	53815	87055	30429
8	181069	53046	105878	34218
9	840711	243529	433861	145737

Table 4.11: The number of the streamlines of the right and the left hemispheres using deterministic method for cases 5, 6, 7, 8, 9.

Deterministic				
Case	Right		Left	
	FA=0,2	FA=0,4	FA=0,2	FA=0,4
5	79531	22895	73357	21041
6	66531	17895	57981	11473
7	89542	26512	82219	23960
8	83534	24116	83801	25131
9	412729	103339	426629	133735

Table 4.12: The number of the streamlines of the right and the left hemispheres using deterministic method for cases 5, 6, 7, 8, 9.

Probabilistic				
Case	Right		Left	
	FA=0,2	FA=0,4	FA=0,2	FA=0,4
5	39801	13759	36019	12926
6	36189	10883	32835	7275
7	43528	14789	40391	13317
8	48108	15444	56785	17443
9	206457	59734	221998	80737

Conclusion

The presented study was conducted with the aim of obtaining a better reconstruction of the damaged region in the brain. For that purpose, we used the data obtained from the diffusion MRI technique and transformed then into the format accepted by the Dipy community.

In the performed experiment we used the Constrained Spherical Deconvolution (CSD) reconstruction technique to overcome the crossing fibers limitation and obtain a more realistic view of the brain's fibers architecture. Subsequently we used both probabilistic and the deterministic tractography algorithms with two values of fractional anisotropy namely FA=0.2 and FA=0.4 as stopping criteria for each algorithm.

To decide the better algorithm to utilize, we first analysed the streamlines of the whole brain in the files obtained from the four programs.

The first remark was that the number of streamlines using FA=0.2 as stopping criterion is greater than the number of streamlines using FA=0.4 which was expected before the test and this is because when we increase the fractional anisotropy we recover only the fibers with high diffusivity as fibers in "corpus collosum".

The second remark is that the number of streamlines using the same FA is greater while using the deterministic algorithm , which is explained as follow:

"The probabilisitc algorithm connects more voxels and that generates less streamlines but with higher lengths" that was confirmed using an option in the MI-brain platform that can filter the streamlines according to their lengths, and that was done by increasing the min_ length of the fibers and we noticed the opposite (number of streamlines generated by the probabilistic becomes larger) we can conclude that the probabilistic algorithm gives more realistic view of the brain.

The second step was analysing the right and the left hemispheres and we found that

using FA=0.4 the number of streamlines is less in the damaged hemisphere than in the non-damaged hemisphere but using FA=0.2 the number of streamlines of the damaged hemisphere is greater and this can be explained as follow :

The fibers in the surrounding region of the tumor are cut and of low diffusivity and this was concluded from analysing the ROI using MI-brain.

For more information we used segmentation to extract the tumor and study the performance of the four used algorithms in the ROI. We noticed that the probabilistic method gives more information concerning the ROI we noticed also that in some cases the tract enters inside the tumor but in other cases it stops before entering and this is related to the type of the disease.

From all results we can confirm that the probabilistic method provides more information about the damaged region.

Bibliography

[1] Peter J Basser and Carlo Pierpaoli. A simplified method to measure the diffusion tensor from seven mr images. *Magnetic resonance in medicine*, 39(6):928–934, 1998.

[2] Robert Brown. Xxvii. a brief account of microscopical observations made in the months of june, july and august 1827, on the particles contained in the pollen of plants; and on the general existence of active molecules in organic and inorganic bodies. *The Philosophical Magazine*, 4(21):161–173, 1828.

[3] Dalila Cherifi, Messaoud Boudjada, Abdelatif Morsli, Gabriel Girard, and Rachid Deriche. Combining improved euler and runge-kutta 4th order for tractography in diffusion-weighted mri. *Biomedical Signal Processing and Control*, 41:90–99, 2018.

[4] H-W Chung, M-C Chou, and C-Y Chen. Principles and limitations of computational algorithms in clinical diffusion tensor mr tractography. *American Journal of Neuroradiology*, 32(1):3–13, 2011.

[5] Perrine Clarisse. *Tractographie cérébrale par IRM de tenseur de diffusion: influence des paramètres d'acquisition et de la méthode de tractographie sur la reproductibilité et la plausibilité anatomique des résultats dans la perspective d'une application en routine clinique*. PhD thesis, Université de Toulouse, Université Toulouse III-Paul Sabatier, 2008.

[6] Jonathan D Clayden, S Muñoz Maniega, Amos J Storkey, Martin D King, Mark E Bastin, Chris A Clark, et al. Tractor: magnetic resonance imaging and tractography with r. *Journal of Statistical Software*, 44(8):1–18, 2011.

[7] Flavio Dell'Acqua and J-Donald Tournier. Modelling white matter with spherical deconvolution: How and why? *NMR in Biomedicine*, 32(4):e3945, 2019.

[8] Maxime Descoteaux. High angular resolution diffusion imaging (hardi). *Wiley Encyclopedia of Electrical and Electronics Engineering*, pages 1–25, 1999.

[9] Maxime Descoteaux. *High angular resolution diffusion MRI: from local estimation to segmentation and tractography*. PhD thesis, Université Nice Sophia Antipolis, 2008.

[10] Maxime Descoteaux, Elaine Angelino, Shaun Fitzgibbons, and Rachid Deriche. Regularized, fast, and robust analytical q-ball imaging. *Magnetic Resonance in Medicine: An Official Journal of the International Society for Magnetic Resonance in Medicine*, 58(3):497–510, 2007.

[11] Adolph Fick. On liquid diffusion. *Journal of Membrane Science*, 100(1):33–38, 1995.

[12] Abebe Geletu. Introduction to differential algebraic equations. *Ilmenau University of Technology, Department of Simulation and Optimal Processes (SOP), Winter Semester*, 12, 2011.

[13] Christopher P Hess, Pratik Mukherjee, Eric T Han, Duan Xu, and Daniel B Vigneron. Q-ball reconstruction of multimodal fiber orientations using the spherical harmonic basis. *Magnetic Resonance in Medicine: An Official Journal of the International Society for Magnetic Resonance in Medicine*, 56(1):104–117, 2006.

[14] Ben Jeurissen, Maxime Descoteaux, Susumu Mori, and Alexander Leemans. Diffusion mri fiber tractography of the brain. *NMR in Biomedicine*, 32(4):e3785, 2019.

[15] Bruno Jobard and Wilfrid Lefer. Creating evenly-spaced streamlines of arbitrary density. In *Visualization in Scientific Computing'97*, pages 43–55. Springer, 1997.

[16] Heidi Johansen-Berg and Timothy EJ Behrens. *Diffusion MRI: from quantitative measurement to in vivo neuroanatomy*. Academic Press, 2013.

[17] Denis Le Bihan, Eric Breton, Denis Lallemand, Philippe Grenier, Emmanuel Cabanis, and Maurice Laval-Jeantet. Mr imaging of intravoxel incoherent motions: application to diffusion and perfusion in neurologic disorders. *Radiology*, 161(2):401–407, 1986.

[18] Michael Quellmalz. A generalization of the funk–radon transform. *Inverse Problems*, 33(3):035016, 2017.

[19] Kiran Kumar Seunarine. *Estimating uncertainty in multiple fibre reconstructions*. PhD thesis, UCL (University College London), 2011.

[20] Edward O Stejskal and John E Tanner. Spin diffusion measurements: spin echoes in the presence of a time-dependent field gradient. *The journal of chemical physics*, 42(1):288–292, 1965.

[21] J-Donald Tournier, Fernando Calamante, and Alan Connelly. Robust determination of the fibre orientation distribution in diffusion mri: non-negativity constrained super-resolved spherical deconvolution. *Neuroimage*, 35(4):1459–1472, 2007.

[22] David S Tuch. Q-ball imaging. *Magnetic Resonance in Medicine: An Official Journal of the International Society for Magnetic Resonance in Medicine*, 52(6):1358–1372, 2004.

[23] Anh Tu Van, Cristina Granziera, and Roland Bammer. An introduction to model-independent diffusion mri. *Topics in magnetic resonance imaging: TMRI*, 21(6):339, 2010.

[24] Zhanxiong Wu. A new method of tracking of wm crossing fiber bundles based on qbi. *Engineering*, 5(10):250, 2013.

Appendices

A Tensor estimation

From equation 2.3, we get :

$$g^T Dg = -\frac{\ln\left(\frac{S}{S_0}\right)}{b} \tag{.1}$$

By replacing g and D in .1 we get:

$$\begin{pmatrix} g_x & g_y & g_z \end{pmatrix} \begin{pmatrix} D_{xx} & D_{xy} & D_{xz} \\ D_{yx} & D_{yy} & D_{yz} \\ D_{zx} & D_{zy} & D_{zz} \end{pmatrix} \begin{pmatrix} g_x \\ g_y \\ g_z \end{pmatrix} = -\frac{\ln\left(\frac{S}{S_0}\right)}{b} \tag{.2}$$

The right side of equation .1 can be expanded as follow :

$$g^T Dg = g_x^2 D_{xx} + g_y^2 D_{yy} + g_z^2 D_{zz} + 2g_x g_y D_{xy} + 2g_x g_z D_{xz} + 2g_y g_z D_{yz} \tag{.3}$$

Now replacing equation .3 in (.2), we get:

$$g_x^2 D_{xx} + g_y^2 D_{yy} + g_z^2 D_{zz} + 2g_x g_y D_{xy} + 2g_x g_z D_{xz} + 2g_y g_z D_{yz} = -\frac{\ln\left(\frac{S_k}{S_0}\right)}{b} \tag{.4}$$

S_k, S_0, g_k are all known, and since we have six unknown parameters of diffusion tensor, we need M applied gradient where $M > 6$.

Finally we get :

$$g_i^T Dg_i = -\frac{\ln\left(\frac{S_i}{S_0}\right)}{b} \ , \qquad i \in 1, ..., M \tag{.5}$$

$$\begin{pmatrix} g_{1,x}^2 & g_{1,y}^2 & g_{1,z}^2 & 2g_{1,x}g_{1,y} & 2g_{1,x}g_{1,z} & 2g_{1,y}g_{1,z} \\ .. & .. & .. & .. & .. & .. \\ g_{M,x}^2 & g_{M,y}^2 & g_{M,z}^2 & 2g_{M,x}g_{M,y} & 2g_{M,x}g_{M,z} & 2g_{M,y}g_{M,z} \end{pmatrix} \begin{pmatrix} D_{xx} \\ D_{yy} \\ D_{zz} \\ D_{xy} \\ D_{xz} \\ D_{yz} \end{pmatrix} = \frac{-1}{b_i} \begin{pmatrix} \ln\left(\frac{S_1}{S_0}\right) \\ . \\ . \\ . \\ \ln\left(\frac{S_M}{S_0}\right) \end{pmatrix} \tag{.6}$$

To solve for diffusion tensor parameters we apply the Linear Least Square method equation .7 to equation .6

$$x^* = \left(A^T A\right)^{-1} A^T Y \tag{.7}$$

where:

$$x^* = \begin{pmatrix} D_{xx} \\ D_{yy} \\ D_{zz} \\ D_{xy} \\ D_{xz} \\ D_{yz} \end{pmatrix}$$

$$A = \begin{pmatrix} g_{1,x}^2 & g_{1,y}^2 & g_{1,z}^2 & 2g_{1,x}g_{1,y} & 2g_{1,x}g_{1,z} & 2g_{1,y}g_{1,z} \\ .. & .. & .. & .. & .. & .. \\ g_{M,x}^2 & g_{M,y}^2 & g_{M,z}^2 & 2g_{M,x}g_{M,y} & 2g_{M,x}g_{M,z} & 2g_{M,y}g_{M,z} \end{pmatrix}$$

$$Y = \frac{-1}{b_i} \begin{pmatrix} \ln\left(\frac{S_1}{S_0}\right) \\ . \\ . \\ . \\ \ln\left(\frac{S_M}{S_0}\right) \end{pmatrix}$$

B Acquistion and reconstruction techniques figures

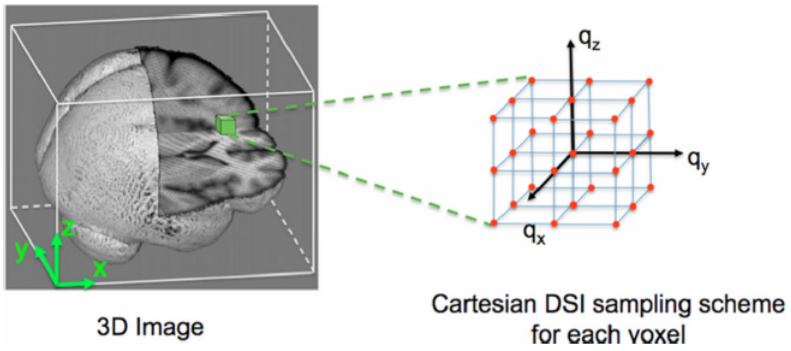

Figure 15: 3D Cartesian sampling scheme of diffusion spectrum imaging for a single voxel. The red dots indicate the q-values used in the acquisition.

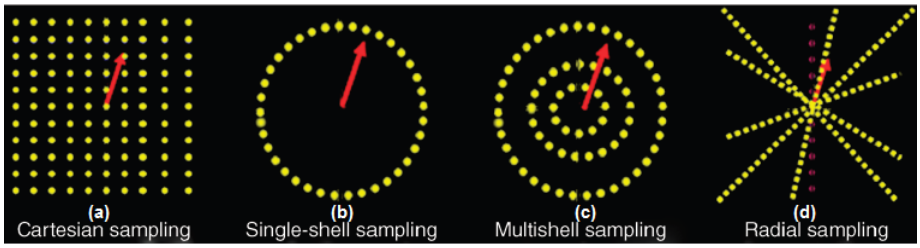

Figure 16: Sampling schemes in q-space. (a) Cartesian sampling dedicated to diffusion spectrum imaging (DSI). (b) Single-shell spherical sampling dedicated to HARDI. (c) Multiple shell spherical sampling and (d) Radial sampling schemes dedicated to advanced diffusion propagator imaging and compartment modeling.

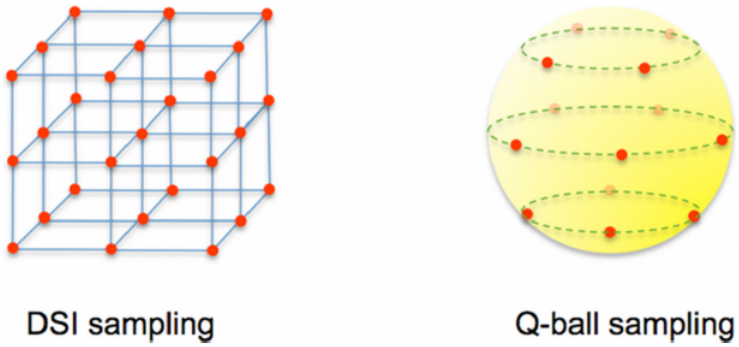

Figure 17: Sampling strategies for DSI and q-ball .

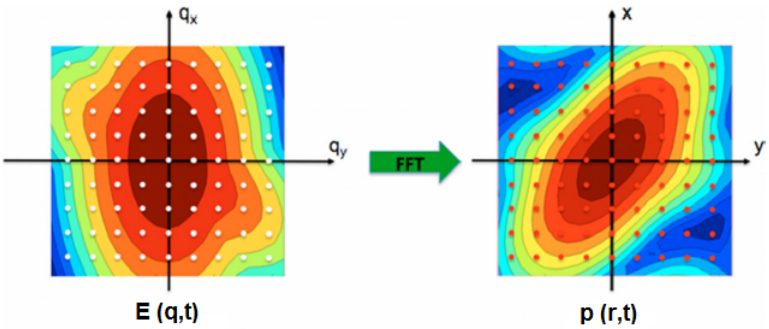

Figure 18: 2D illustration for estimating PDF $p(r,t)$ for a single voxel; white dots on $E'q,t)$ show the q-space location at which a measurement is obtained and the red dots grid on $p(r,t)$ are obtained by the Fourier transform of the white dots.

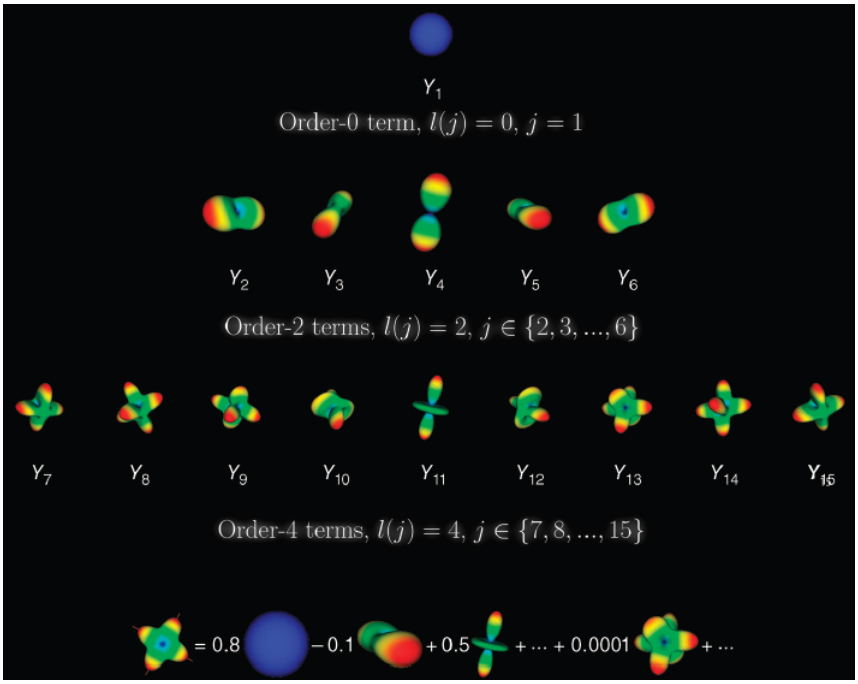

Figure 19: Spherical harmonics basis.

C Tractography figures

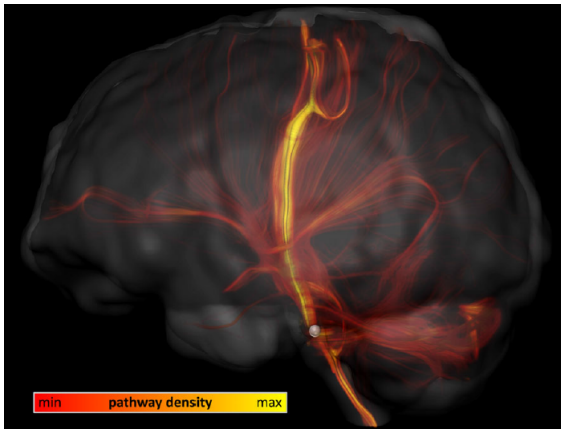

Figure 20: Probabilistic streamlines emanating from a single seed point (white sphere). The trajectories are colored according to the local density of the trajectories [14].

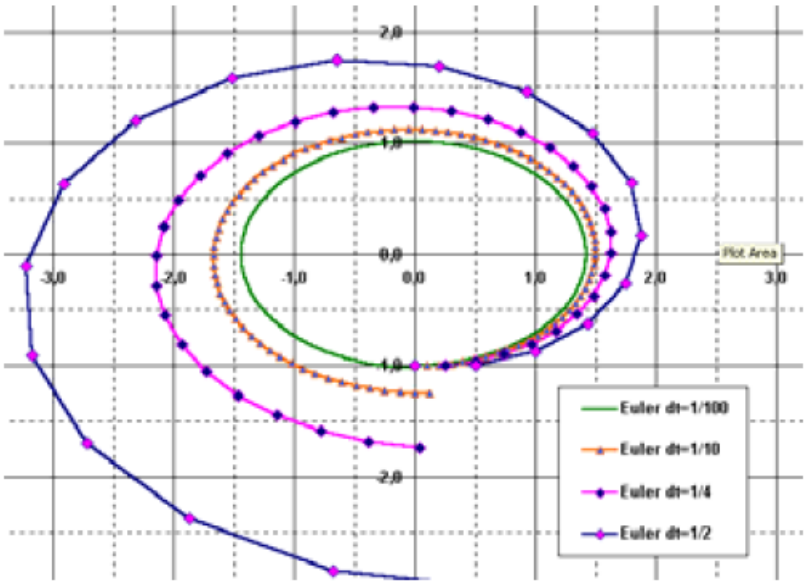

Figure 21: Example of Euler integration method with different step sizes .

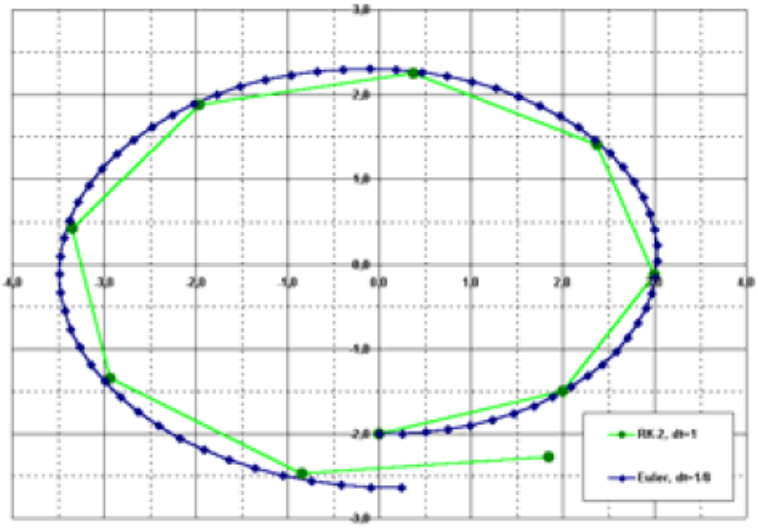

Figure 22: Runge Kutta 2 with 9 steps better than Euler with 72 step .

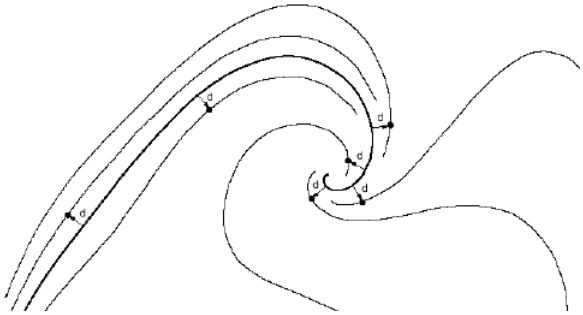

Figure 23: Distance between streamlines.

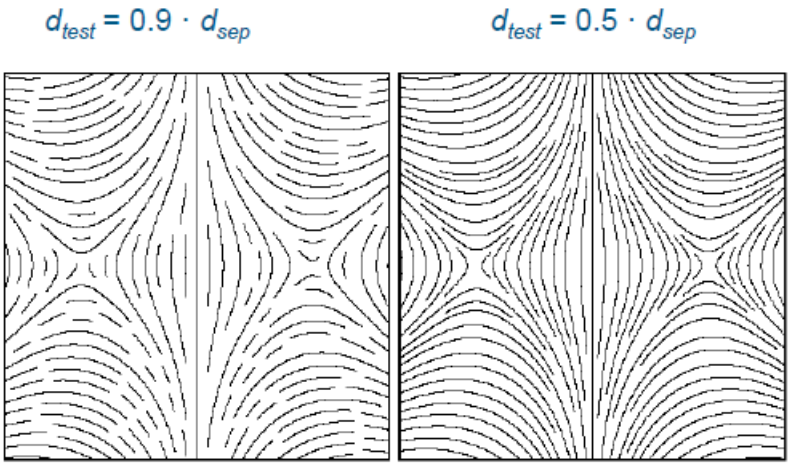

Figure 24: d_{test} vs d_{sep}.